metals

MDPI

Article

Influence of Substrate Preheating on Processing Dynamics and Microstructure of Alloy 718 Produced by Directed Energy Deposition Using a Laser Beam and Wire

Atieh Sahraeidolatkhaneh *, Achmad Ariaseta, Gökçe Aydin, Morgan Nilsen and Fredrik Sikström

Department of Engineering Science, University West, 46186 Trollhättan, Sweden; achmad.ariaseta@hv.se (A.A.); gokce.aydin@hv.se (G.A.); morgan.nilsen@hv.se (M.N.); fredrik.sikstrom@hv.se (F.S.)
* Correspondence: atieh.sahraeidolatkhaneh@hv.se

Abstract

Effective thermal management is essential in metal additive manufacturing to ensure process stability and desirable material properties. Directed energy deposition using a laser beam and wire (DED-LB/w) enables the production of large, high-performance components but remains sensitive to adverse thermal effects during multi-layer deposition due to heat accumulation. While prior studies have investigated interlayer temperature control and substrate preheating in DED modalities, including laser-powder and arc-based systems, the influence of substrate preheating in DED-LB/w has not been thoroughly examined. This study employs substrate preheating to simulate heat accumulation and assess its effects on melt pool geometry, wire–melt pool interaction, and the microstructural evolution of Alloy 718. Experimental results demonstrate that increased substrate temperatures lead to a gradual expansion of the melt pool, with a notable transition occurring beyond 400 °C. Microstructural analysis reveals that elevated preheat temperatures promote coarser secondary dendrite arm spacing and the development of wider columnar grains. Moreover, Nb-rich secondary phases, including the Laves phase, exhibit increased size but relatively unchanged area fractions. Observations from electrical conductance measurements and coaxial visual imaging show that preheat temperature significantly affects the process dynamics and microstructural evolution, providing a basis for advanced process control strategies.

Keywords: directed energy deposition; DED-LB/w; substrate preheating; melt pool; melt pool-wire interaction; Alloy 718; microstructural evolution

check for updates

Academic Editors: Peng Dong and Zhifeng Yan

Received: 23 September 2025
Revised: 20 October 2025
Accepted: 23 October 2025
Published: 25 October 2025

Citation: Sahraeidolatkhaneh, A.; Ariaseta, A.; Aydin, G.; Nilsen, M.; Sikström, F. Influence of Substrate Preheating on Processing Dynamics and Microstructure of Alloy 718 Produced by Directed Energy Deposition Using a Laser Beam and Wire. *Metals* **2025**, *15*, 1184. https://doi.org/10.3390/met15111184

Copyright: © 2025 by the authors. Licensee MDPI, Basel, Switzerland. This article is an open access article distributed under the terms and conditions of the Creative Commons Attribution (CC BY) license (https://creativecommons.org/licenses/by/4.0/).

1. Introduction

Metal additive manufacturing (AM) has transformed modern manufacturing by enabling the production of complex components with high precision and better process flexibility [1]. Directed energy deposition using a laser beam and wire (DED-LB/w) is one of the AM techniques that can produce customizable large-scale parts with less material waste, making it particularly valuable in industries like aerospace [2]. A laser beam melts a metal feedstock wire in DED-LB/w, allowing the molten metal to flow from the wire to a melt pool produced on either a substrate or a previously deposited layer. Metal transfer dynamics have a significant impact on the overall performance of this process [3]. As a result, measuring the electrical conductivity from an injected current through the feedstock wire to the melt pool offers vital information about the transition of the solid wire to the molten region [4].

Despite the advantages of this method, heat accumulation during multi-layer deposition remains a major challenge. In layer-by-layer deposition techniques like DED-LB/w, repeated thermal cycles lead to heat accumulation, raising the preheating temperature of previously deposited layers [5]. The combination of high energy density and high deposition rate [5,6] exacerbates this issue, causing fluctuations in melt geometry that lead to deviations from the intended geometry and part accuracy. Additionally, the increase in preheating temperature influences cooling rates, resulting in the heterogeneity of microstructure and mechanical properties of as-built components. Halder et al. [6] reported that heat accumulation due to variations in interlayer times influences melt pool geometry, the size of the solidified microstructure, i.e., the thickness of alpha lath, and the hardness of the Ti-6Al-4V deposited by DED-LB/w. Simulations and experiments in [7] revealed that process quality depends on controlling parameters such as interlayer times, resulting in less built deformation while improving build efficiency. In directed energy deposition using wire arc (DED-Arc), studies by several researchers [8–12] have shown that managing heat accumulation through interlayer time control is an effective approach for optimizing geometry, microstructure, and mechanical performance. In other studies [13–16], the accumulation of heat due to a lack of interlayer time control caused by an increase in the number of deposited layers resulted in larger grain sizes and bead dimensions due to varying cooling rates. These results demonstrated how crucial it is to maintain stringent interlayer temperature control to guarantee sound deposition and reliable part quality. Thus, managing heat accumulation is of utmost importance to ensure high-quality parts [17].

One approach to studying the impact of heat accumulation in the previously deposited layers on the geometry and microstructure of subsequent layers is through single bead-on-plate deposition on substrates preheated to different temperatures. By adjusting the substrate's initial preheat temperature, one can simulate varying interlayer temperatures during multi-layer deposition. The influence of preheated substrates on the microstructure and mechanical properties of Alloy 718 has been addressed in the DED-LB employing powder feedstock (DED-LB/p) by Jin et al. [18]. Their findings showed that substrate preheating significantly reduced the temperature gradient and cooling rate, resulting in coarser solidified microstructures and increasing the melt pool depth and width by more than 10%. Alloy 718 is a Niobium (Nb)-bearing Nickel-Iron (Ni-Fe)-based superalloy primarily strengthened by γ'' (Ni3Nb) phase for elevated temperature applications up to 650 °C [19]. It is one of the most widely used superalloys in high-temperature structural components of aircraft engines, and it has gained significant interest in DED-LB/w applications owing to its excellent weldability in terms of immunity to strain age cracking [20].

Due to the sluggish precipitation of γ'' relative to γ'' (Ni3(AlTi)) phase, Alloy 718′s excellent resistance to strain age cracking is beneficial from an AM processability (printability) standpoint, especially during multi-layer deposition where the buildup of thermal residual stresses occurs in the solidified layers and the previous layers become heat-affected zones and are exposed for a particular time to the age hardening temperature range.

To the best of the author's knowledge, studies on the influence of heat accumulation during AM processes were mainly reported on titanium alloys and steels, with most of them focusing on the DED-Arc and/or DED-LB/p processes. Previous research has not addressed how heat accumulation affects the melt pool, melt pool-wire interaction behavior, and microstructure of Alloy 718 during the DED-LB/w process.

This study seeks to examine the influence of substrate preheating, which replicates the effect of elevated interlayer temperatures caused by heat accumulation, on the melt pool geometry, the melt pool-wire interaction, and microstructure of Alloy 718 produced via single-track bead-on-plate DED-LB/w. The objective is to utilize this knowledge to

mitigate the adverse effects of heat accumulation and stabilize process dynamics by in-process monitoring. Furthermore, the acquired knowledge will aid in developing strategies to control heat and mass transfer, thereby enhancing bead geometry and minimizing thermal gradients. The findings are anticipated to offer valuable insights for optimizing process parameters and establishing automated control schemes to improve the quality and reliability of Alloy 718 deposits in DED-LB/w.

2. Materials and Methods

This section describes the experimental and monitoring setup used during the deposition of single beads, including the process imaging and electrical conductance measurements. In addition, metallographic and microstructural evaluations were performed to identify the characteristics of the deposited beads.

2.1. DED-LB/w Processing Setup

The deposition experiments were conducted using a DED-LB/w system, as shown in Figure 1. The system featured a processing head mounted on the arm of a six-axis industrial robot IRB-4400 (ABB Robotics, Västerås, Sweden), which provided high-precision motion control. The collimated laser beam was directed onto the substrate through a dichroic mirror and subsequently focused to create a defined interaction zone. To minimize oxidation, all experiments were performed within a shielding gas tent filled with argon, with an oxygen level less than 50 ppm. The processing head, supplied by Permanova Laser System AB (Permanova Lasersystem AB, Mölndal, Sweden) [21], included a 300 mm focal lens and a 60 mm collimation lens, yielding a magnification factor of five. Laser power was transmitted to the processing head through a 1000 µm diameter optical fiber, producing a laser beam spot with a 5 mm diameter and a top-hat power density distribution. The laser source used in these experiments was a Trumpf TruDisk 12002 (Trumpf SE + Co. KG, Ditzingen, Germany), operating at a wavelength of 1030 nm. A copper nozzle was attached to the processing head, directing the feedstock wire into the interaction zone between the laser beam and the melt pool. Additionally, the nozzle served as the positive terminal, acting as the electrical contact to enable current flow through the wire. An electrical current was sent through the wire, allowing it to pass through the wire stick-out, melt pool, and substrate, forming a closed circuit. This circuit was powered by a low-current DC voltage source [22]. The electrical conductance was determined by measuring the voltage drop and the current, following the reciprocal of Ohm's law. The setup included a T drive 4 Rob 3 feedstock wire feeder (EWM AG, Mündersbach, Germany) and an AM8131 servo-drive (Beckhoff Automation GmbH & Co. KG, Verl, Germany). Actuator control and communication with the industrial robot were managed using a CX9020 PLC (Beckhoff Automation GmbH & Co. KG, Verl, Germany).

A high-speed CMOS camera CCM-1540 (Integrated Design Tools Inc., Pasadena, CA, USA) was positioned off-axis, facing the substrate, to capture side-views of the wire's contact with the melt pool, Figure 2a. Images were recorded using Motion Studio x64 software (Integrated Design Tools Inc., Pasadena, CA, USA) at 800 fps with a 29 µs exposure time and a resolution of 1344 × 760 pixels. A blue LED lamp (Thorlabs Inc., Town of Newton, NJ, USA) (450 nm) was employed for back-lit illumination to acquire the shape of the wire when entering the melt pool, see Figure 2a.

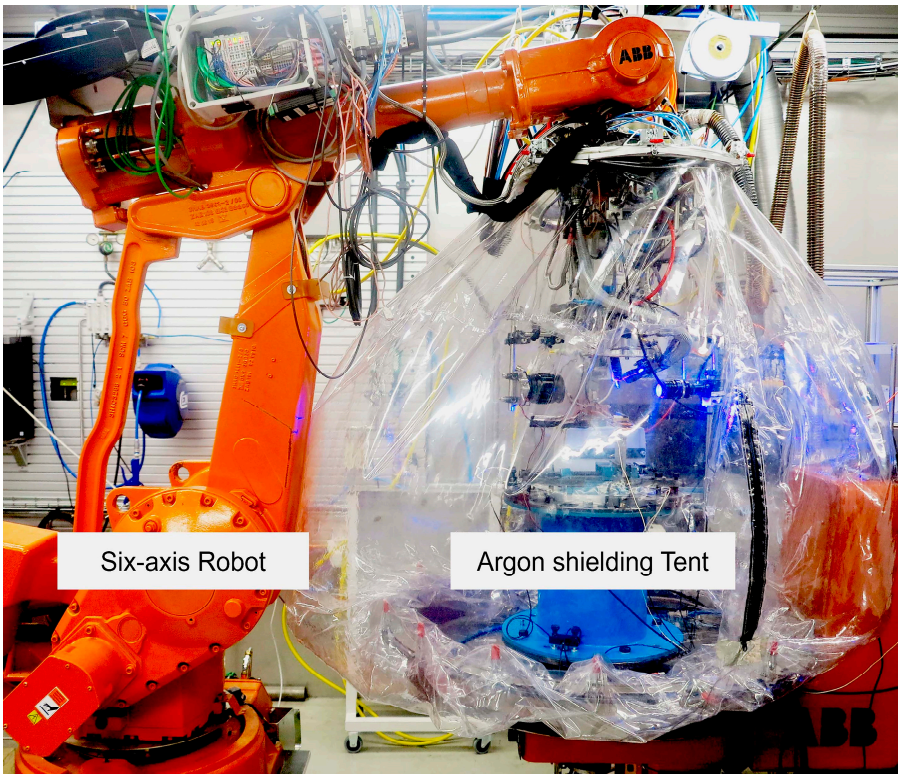


Figure 1. Robotized DED-LB/w cell with shielding gas tent, safety system, and industrial controllers.

A second camera was used coaxially with the processing laser beam to observe the top surface of the melt pool. Example images captured using the high-speed camera and coaxial camera are presented in Figure 3. In images captured from the off-axis camera, the wire entered the view from the right, and it is positioned at an angle to the substrate/melt pool, see Figure 3a. In the top-view image, the tip of the wire can be seen, which is surrounded by the melt pool, see Figure 3b.

2.2. Processing Parameters

Throughout the tests, single bead deposits were produced. To eliminate laser beam reflections into the optics during deposition, the processing head was tilted 5° from the normal direction to the substrate's surface. An Alloy 718 wire with a diameter of 1.14 mm was utilized to deposit beads on 100 mm × 8.0 mm × 148 mm Alloy 718 substrates. Table 1 shows the chemical compositions of the substrate and wire. Before processing, the substrates were first cleaned, and then the top surface of the substrate was manually polished. Afterward, the substrate was chemically cleaned using acetone. Careful attention was given to programming the start and end points of each bead to ensure that straight and uniform beads were deposited, even in cases where the substrate exhibited slight tilts due to the manual mounting each time. Five beads were produced, during which key processing parameters were held constant to ensure process consistency. The laser power was maintained at 2.5 kW, the travel speed at 10 mm/s, and the wire feed speed at 1.35 m/min, resulting in a conduction mode melting. These processing conditions were determined through preliminary experiments to establish a nominal deposition process. The substrate was preheated before depositing four out of five beads. Table 2 displays the substrate's preheat temperature values from the experiments.

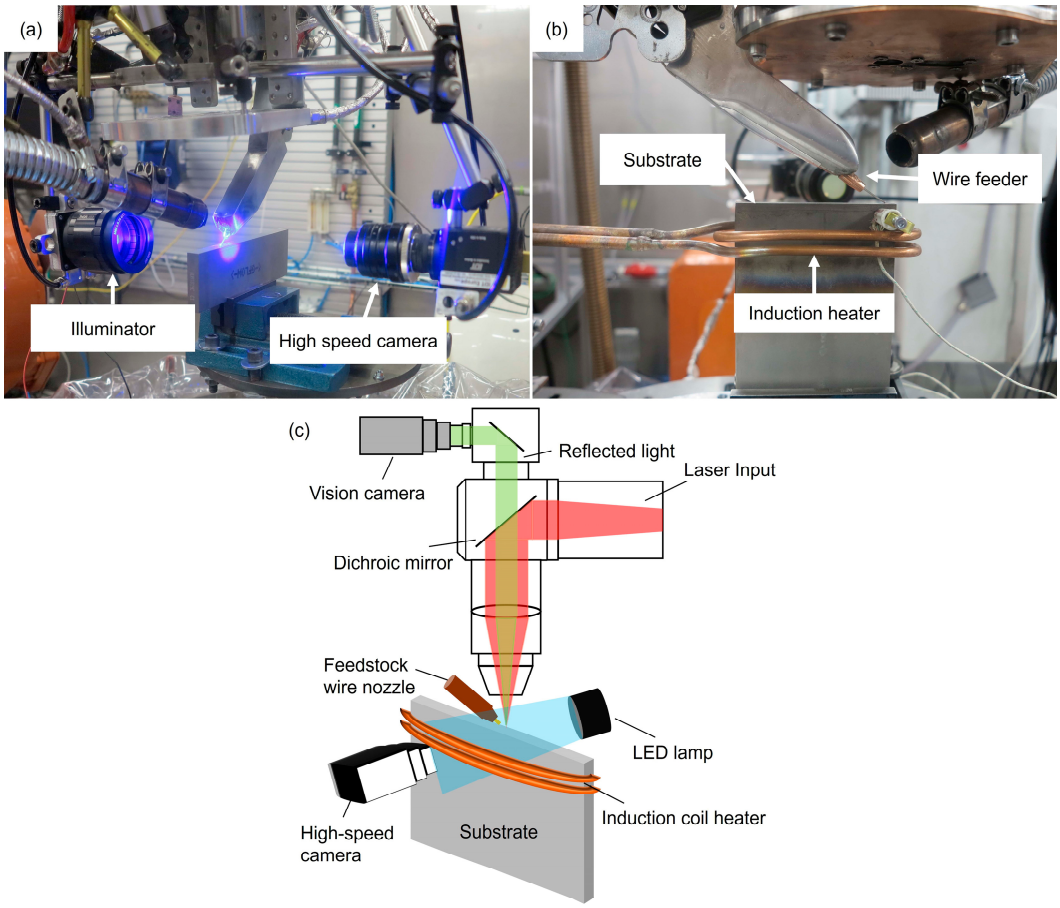


Figure 2. Monitoring and deposition equipment: (**a**) high-speed camera positioned off-axis to the side of the substrate, and the illuminator is placed on the opposite side, (**b**) an induction heater coil surrounded the upper side of the substrate near its top surface, (**c**) Experimental setup showing the DED-LB/w processing head, process monitoring configuration. The induction coil surrounding the substrate represents the induction heating system.

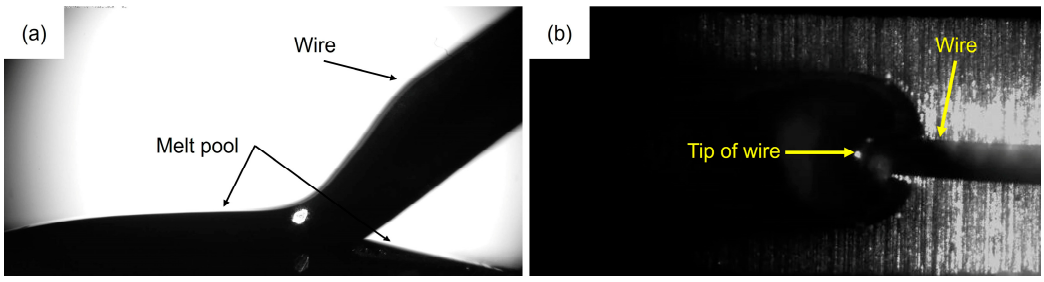


Figure 3. Examples of images acquired during the experiments. (**a**) Side-view image, (**b**) top-view image.

Table 1. Chemical composition (wt%) of substrate and feedstock wire.

Element (wt%)	Ni	Cr	Mo	Cb (Nb)	Ti	Al	Fe	C
Substrate & wire	50.00–55.00	17.00–21.00	2.80–3.30	4.75–5.50	0.65–1.15	0.20–0.80	Balance	0.08 max

Table 2. Levels of substrate preheat temperature.

Experiment Number	1	2	3	4	5
Temperature	25 °C	200 °C	400 °C	600 °C	800 °C

To achieve the desired substrate temperatures, a custom-designed induction heater, with a coil fabricated from copper, was positioned around the substrate, as shown in Figure 2b. The substrate temperature was incrementally increased by 200 °C for each experimental run. Substrate temperatures were controlled by a proportional integral derivative (PID) controller using a thermocouple, ensuring they reached the target values before deposition commenced. The heater was turned off just before the start of a deposition to not impact the temperature evolution from that point in time.

2.3. Data Analysis

2.3.1. Gaussian Process Regression

Gaussian Process Regression (GPR) [23] was utilized to model and predict the melt pool geometry, liquid bridge geometry, bead cross-sectional features, and microstructural characteristics as a function of substrate preheat temperature. The experimental dataset consisted of five input points corresponding to substrate temperatures of 25, 200, 400, 600, and 800 °C. Each input temperature was associated with multiple measured output parameters, including mean values and standard deviations of the features of interest (e.g., melt pool width, conductance, liquid bridge length and width, bead width, height, penetration depth, and total area).

A separate GPR model was trained for each output variable using MATLAB's (R2023b) fitrgp function with a Squared Exponential (SE) kernel, which assumes a smooth underlying functional relationship between the substrate temperature and the measured response. The model employed standardization of the input data to improve numerical stability and 'exact' fitting and prediction, ensuring the posterior distribution was computed analytically without approximation. Noise was implicitly handled by the kernel's noise term.

To evaluate the generalization ability of the model, predictions were generated for unseen substrate temperatures (10, 100, 300, 500, 700, and 820 °C). The predictive mean and variance were obtained directly from the posterior distribution of each GPR model. The 95% confidence intervals (CIs) were then computed using ± 1.96 times the combined predictive and measurement standard deviations. The resulting predictions were plotted alongside the experimental data with error bars representing measured standard deviations, allowing visual comparison of the model's accuracy and uncertainty across temperature ranges.

It is acknowledged that the experimental dataset consists of only five data points, which limits the statistical strength of the GPR model. In this study, the GPR was not intended for interpolation, but rather as a probabilistic regression framework that provides uncertainty-aware interpolation between experimentally observed points. Unlike a conventional trend line or polynomial fit, the GPR model yields confidence intervals derived from the posterior variance, allowing the quantification of prediction uncertainty and the identification of regions where additional experiments would be most informative.

The GPR predictions were validated qualitatively by ensuring that the predicted means followed the physical trends observed in the experiments (e.g., monotonic increase in melt pool width and conductance with preheat temperature) and that the 95% confidence intervals consistently encompassed the measured data points. Thus, in this context, the GPR model served as a tool for uncertainty quantification and process trend visualization, rather than as a generalizable predictive model.

2.3.2. Melt Pool Top Surface Boundary Contour Width

The top-view images from quasi-steady melt pool solid/liquid boundary contours were analyzed to characterize the melt pool surface boundary contour width. The gray scale images were first cropped to only keep relevant features, see Figure 4a. Since the images had low contrast and it was difficult to separate the edges of the melt from the solid

substrate, a gamma correction and sharpening were applied to enhance contrast and edges, as depicted in Figure 4b. A Gabor filter [24] was applied to the gamma corrected images to further improve the different textures with specific orientation to distinguish the true side contour edges of the melt, as depicted in Figure 4c. The Gabor filter in this study utilized a set of predefined wavelength and orientation values [25].

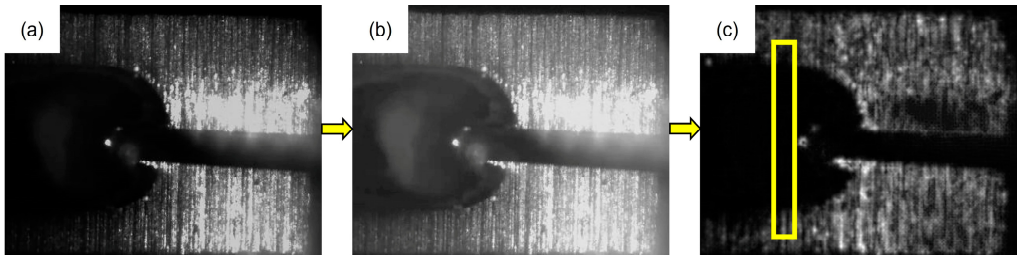


Figure 4. Image processing steps performed on the top-view images: (**a**) Gray-scaled images were cropped, (**b**) a gamma correction followed by image sharpening, (**c**) A specific region was selected on the images filtered by a Gabor filter to identify low-intensity regions.

A specific region was extracted from the filtered image (see Figure 4c), and the intensity sum across rows in this region was computed for each row. To identify low-intensity regions that represent the upper and lower edges of the melt pool, a threshold was set at 1.7 times the minimum value in this range. The selected region to identify these low-intensity regions is shown in Figure 4c. Rows where the intensity fell below this threshold were considered part of the low-intensity region. The start and end indices of the low-intensity region were determined using the first and last occurrences of values below the threshold, see Figure 5. The distance between these indices quantified the melt pool width.

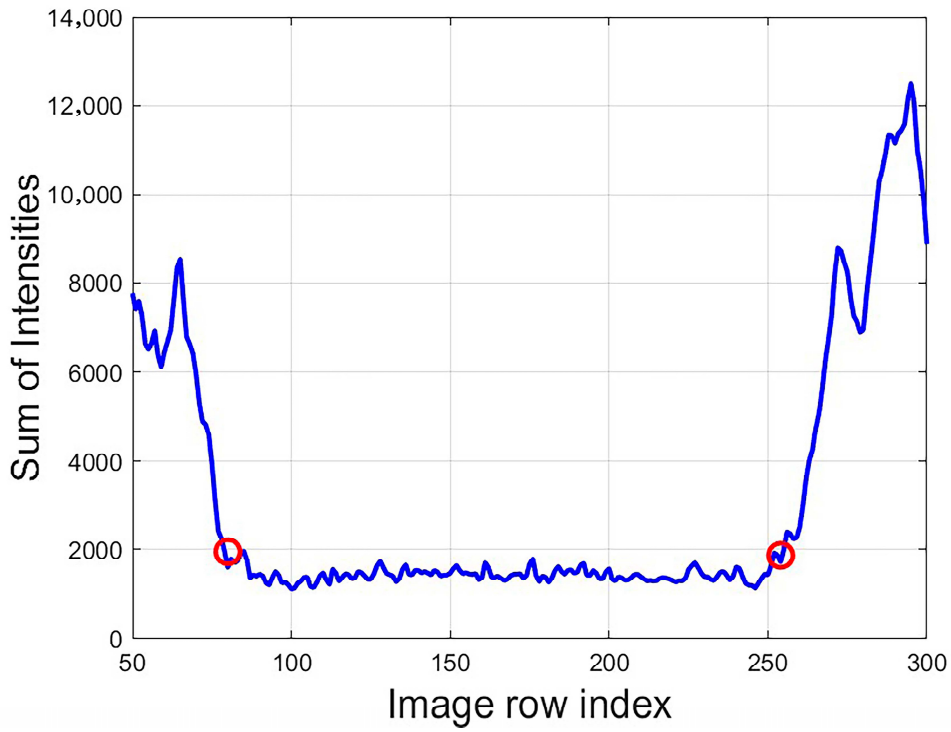


Figure 5. Sum of intensities of rows in the specific region for melt pool width estimation. The red circles quantify the melt pool width.

2.3.3. Liquid Bridge Geometry

The liquid bridge refers to the localized reduction (necking) in wire diameter as it interacts with the laser beam projection and liquid melt pool. This phenomenon can significantly impact the consistency of the metal transfer, as excessive thinning of the wire may lead to wire detachment and formation of droplets, whereas the absence of wire melting can result in solid-to-solid contact with the solid substrate called stubbing [4]. Therefore, monitoring changes in the liquid bridge is important to improve the consistency of the deposition. To characterize the liquid bridge condition, side-view images of the wire boundary contour were analyzed. The method utilized was like that described in [26], and included image selection, contour point identification, convex hull generation, and metrics calculation. A total of 30 images were chosen from about 6800 using a systematic sampling approach to ensure that the findings were representative of the process. In each image, 4 boundary contour points were selected as depicted in Figure 6a. A convex hull was generated based on these points. From the convex hull, the liquid bridge's length was defined by calculating the distance between the left-most and top-most points of the convex hull. The top-most point is where the liquidation of the wire starts, and the circular solid wire cross-section starts to narrow. The left-most point is where the wire enters the melt pool. The width was determined as the distance between the left-most and bottom-most points of the convex hull, see Figure 6b. Then the camera detector pixel coordinates were converted into world coordinates.

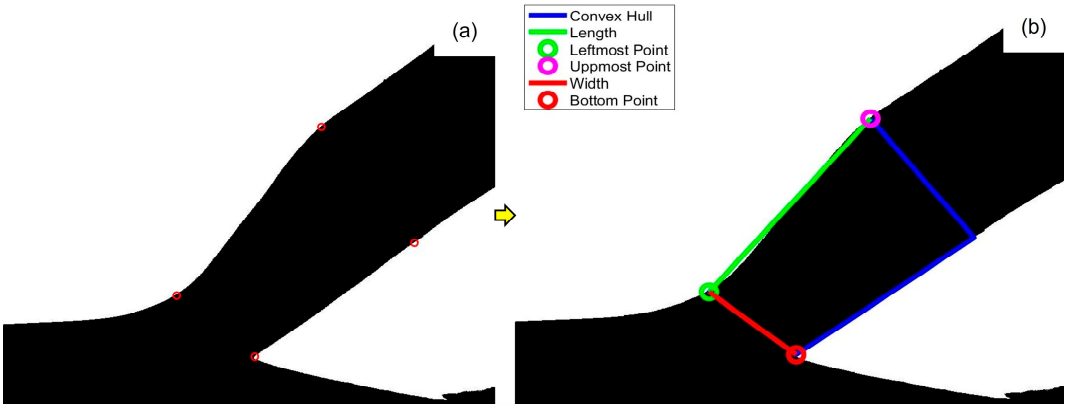


Figure 6. Quantification of the liquid bridge geometry: (**a**) selected boundary contour points used for analysis, (**b**) convex hull generated from the selected points, showing the definitions of the liquid bridge length (distance between top-most and left-most points) and width (distance between left-most and bottom-most points).

2.3.4. Bead Cross-Section Geometry

The as-built beads, see Figure 7a, were sectioned and polished. Subsequently, the etching procedure was performed on the specimens. The geometric features, height, width, penetration depth, area of deposited metal on top, and penetration area were investigated using the inbuilt software in the Zeiss Axio Imager M2m optical microscope (OM) (Carl Zeiss AG, Oberkochen, Germany), as shown in Figure 7b. For each experiment, three cross-sections were prepared. The average and standard deviation of three cross-section measurements were used to investigate the geometrical changes.

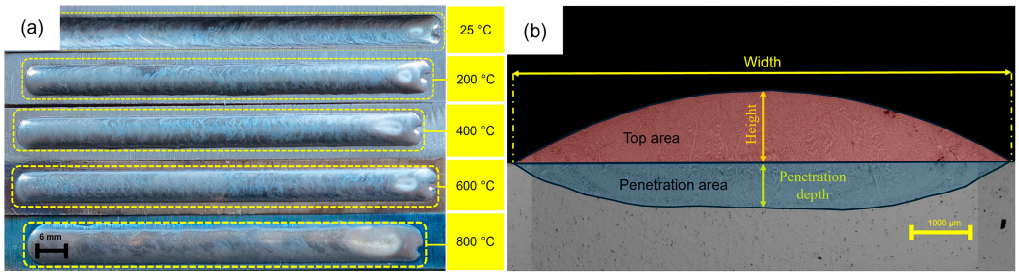


Figure 7. (**a**) As-deposited beads from the different preheating temperatures, (**b**) Geometric features measured in a cross-section (preheat temperature 25 °C).

2.3.5. Microstructural Characterization

Transverse cross-sections of all beads were excised, mounted, and ground using standard metallographic preparation procedures. After grinding, the samples were polished using diamond suspensions and colloidal silica. Electrolytic etching using 10% oxalic acid was then performed on all samples with 2.3 V for 2 s. Microstructures of all samples were examined using a Zeiss Axio Imager M2m optical microscope (Carl Zeiss AG, Oberkochen, Germany) and Zeiss Gemini field-emission gun scanning electron microscope (FEG-SEM) (Carl Zeiss AG, Oberkochen, Germany) that was equipped with Oxford energy dispersive spectroscopy (EDS) and electron backscatter diffraction (EBSD) detectors.

2.3.6. Hardness Testing

Vickers hardness measurements were performed using Struers Duramin-40 (Struers A/S, Ballerup, Denmark). Seven indentations were carried out at the middle of deposition for each condition with an applied load of 500 g (HV0.5) and 10 s dwell time, and the distance between the indentations was 0.25 mm.

2.3.7. Material Modeling

Material modeling using JMatPro (version 6.2.1) software was carried out to calculate the alloy's continuous cooling transformation (CCT) diagram.

3. Results and Discussion

3.1. Imaging and Electrical Conductance Measurements

Figure 8 depicts the melt pool width along the deposition length, revealing a monotonic increase with rising preheat temperature. At 25 °C, the melt pool width is at its minimum, averaging 4.7 mm. As the preheat temperature increases, the width expands, reaching its maximum at 800 °C, where the mean value exceeds 6.0 mm.

The observed widening of the melt pool is attributed to the diminishing temperature gradient between the melt pool and the surrounding material at elevated temperatures of the substrate. At lower preheat temperatures, a relatively colder substrate provides an efficient conduction pathway that confines the melt pool. At higher temperatures, this gradient weakens, and the temperature-dependent thermal conductivity decreases, reducing the effectiveness of heat dissipation. Consequently, heat accumulates near the melt pool surface and shifts the liquidus isotherms outward, leading to lateral spreading and an increased melt pool width [27].

Between 25 °C and 400 °C, the increase in width is moderate. However, beyond 400 °C, the rate of expansion intensifies, particularly between 600 °C and 800 °C. At 600 °C and 800 °C, the melt pool width is 1.14 and 1.33 times greater than at 400 °C, respectively. This suggests the existence of a critical threshold (~400 °C), beyond which the influence of preheating becomes significantly more pronounced, accelerating melt pool expansion. The standard deviation of the melt pool width across different preheat temperatures remains less

than 0.11 mm. Notably, the standard deviation decreases slightly at higher temperatures, especially at 600 °C (0.085 mm) and 800 °C (0.086 mm), compared to room temperature (0.11 mm). This reduction suggests that higher preheat temperatures contribute to fewer fluctuations of the melt pool width.

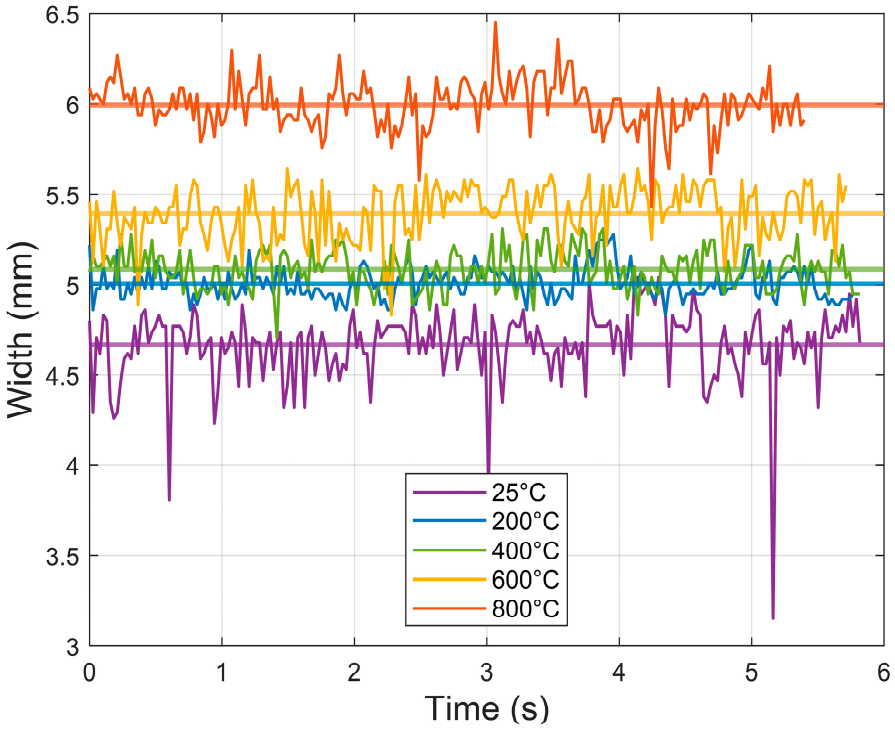


Figure 8. Melt pool width at different preheat temperatures, along with horizontal lines representing their corresponding average values.

Figure 9 shows the change in electrical conductance observed along the depositions at different substrate preheat temperatures. At lower temperatures, 25 °C to 400 °C, the average conductance remains close to each other, showing only a slight decline from 19.1 mS to 18.4 mS. A significant increase in conductance is observed between 400 °C and 600 °C, where the value jumps to 28.7 mS. The conductance reaches its maximum value of 34.4 mS at 800 °C. This shows that the conductance increases with higher temperatures in the selected range due to a larger cross-sectional contact area in the liquid bridge between the wire and molten metal. The slight decrease in conductance predicted in the range between room temperature and 400 °C is not necessarily caused by any significant change in the processing conditions. The data points in this range are all within the confidence interval of the measurements, such that constant conductance is also likely.

The standard deviation remains relatively low across all temperature conditions, ranging from 0.89 mS to 1.34 mS. The lower standard deviation at higher temperatures (600 °C and 800 °C) indicates a steadier melt pool/steadier metal transfer. Qualitative inspection of side-view image sequences (25 representative images per preheat temperature) provided additional context. At 25 °C, short detachment of the wire from the melt pool and pronounced forward-backward oscillations were observed. At 200 °C and 400 °C, the metal transfer became noticeably steadier, with continuous liquid-bridge and minimal oscillation, consistent with the reduced standard deviation of the conductance and melt-pool width observations. At 800 °C, however, periodic vertical wire motion reappeared, and oxide formation became evident on the bead surface (Figure 7a), indicating that although the electrical contact was continuous, the thermal environment introduced new sources of disturbance.

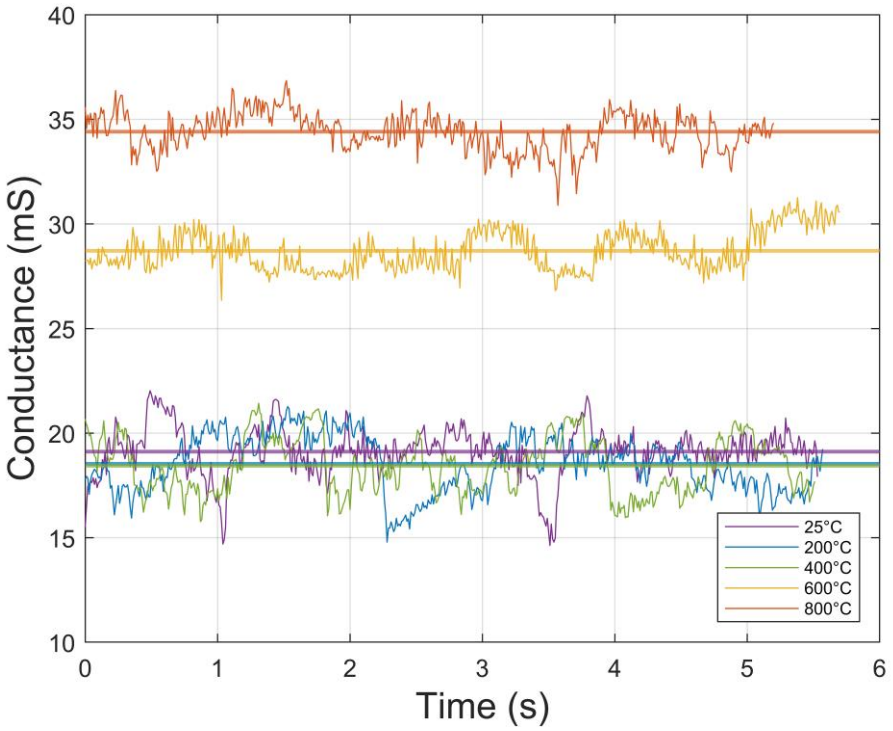


Figure 9. Electrical conductance at different preheat temperatures, along with their average values as horizontal lines.

The liquid bridge (necking) observed in the experiments describes how the wire deforms as it interacts with the laser beam and melt pool. The length (extension of the liquid bridge) and the width (how much the wire thins compared to its original diameter of 1.14 mm) were analyzed at different preheat temperatures. The results show a clear correlation between the temperature and both the extent of the liquid bridge and the smallest width of the liquid bridge (the thinnest section formed during wire deformation), see Figure 10. The average length of the liquid bridge decreases as preheat temperature increases. At 25 °C, the liquid bridge extends the most, reaching an average of 1.33 mm. As the temperature increases, the length gradually reduces to 0.78 mm at 800 °C, which is 40% shorter than at 25 °C.

In case no droplet forms to break the liquid bridge, the wire thins as it melts, but the final liquid bridge width increases as the preheat temperature rises. At 25 °C, the wire thins the most, reaching an average of 0.5 mm, 43% of the original width of the wire. The liquid bridge width gradually increases to 0.65 mm as the temperature increases to 800 °C. At 800 °C, the average liquid bridge width is 57% of the original width, meaning the wire retains more of its thickness at high temperatures.

Figure 11 shows the average melt pool width of each preheat temperature along with the predicted values by the GPR model. The predicted result shows that melt pool width increases consistently with temperature, ranging from 4.79 mm at 100 °C to 5.68 mm at 700 °C. At higher preheat temperatures, the melt pool volume becomes larger and reaches higher temperatures due to the increased heat. Previous research has shown that preheating the substrate leads to a slower cooling rate, resulting in a larger melt pool volume. Additionally, as the substrate temperature increases, the molten metal remains in a liquid state longer [18].

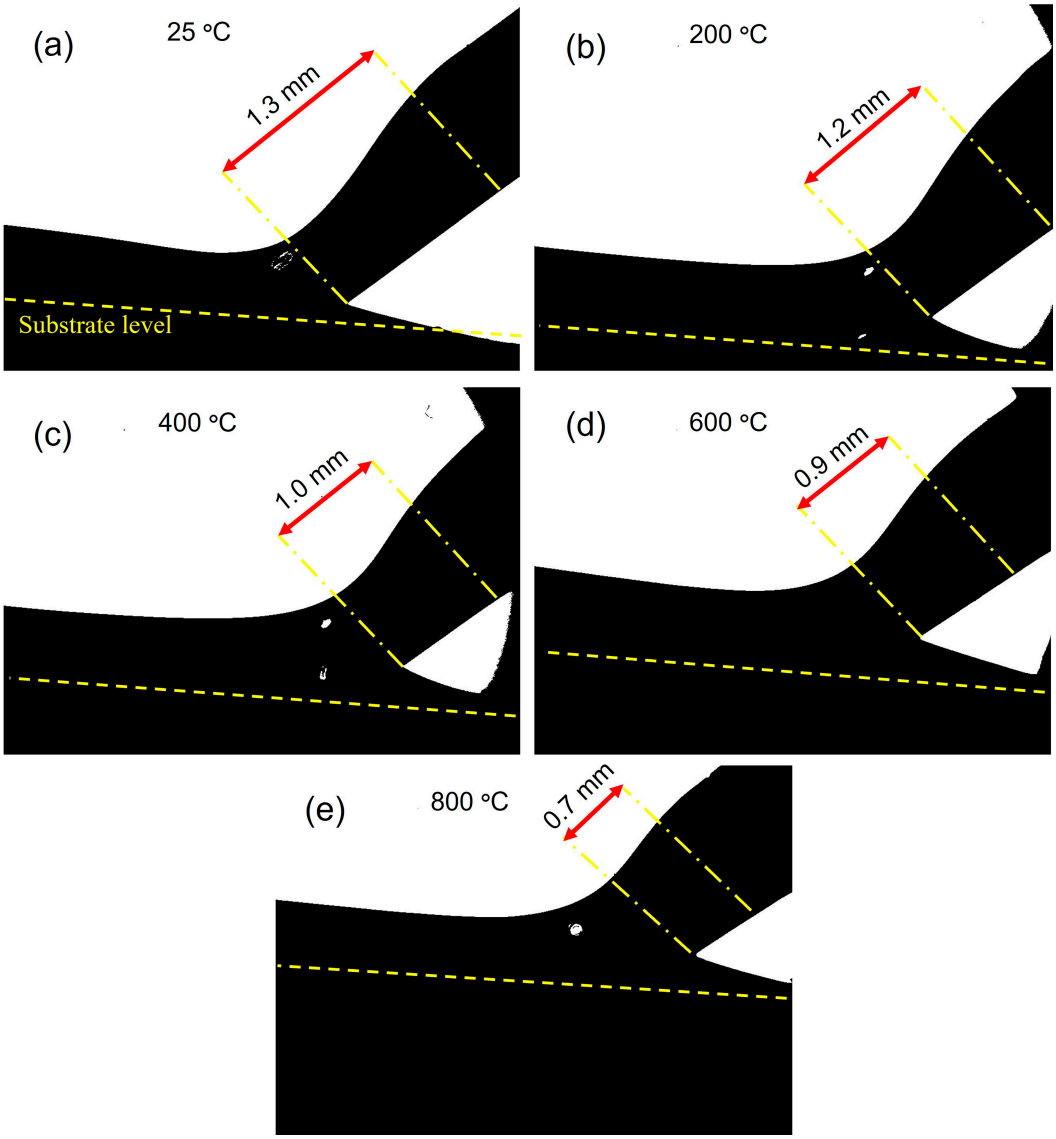


Figure 10. Side-view imaging of the wire-melt pool interconnection showing the influence of substrate's different preheat temperatures on the liquid bridge. The horizontal dashed line in the figures represents the substrate level: (**a**) example of liquid bridge shape at 25 °C with its average measured length, (**b**) 200 °C, (**c**) 400 °C, (**d**) 600 °C, (**e**) 800 °C.

Figure 11b presents the wire's liquid bridge length and width for the preheat temperatures. Data on length and width of the liquid bridge across various substrate temperatures show an inverse relationship. This pattern shows that as the liquid bridge's length decreases, the liquid bridge's width increases, indicating a shift in wire necking at different temperatures.

The predictions show that the liquid bridge's length decreases as the substrate temperature increases, starting at 1.29 mm at 100 °C and reducing to 0.88 mm at 700 °C. The liquid bridge's width increases as preheat temperature rises, from 0.51 mm at 100 °C to 0.62 mm at 700 °C.

Initially, as the temperature increases from 100 °C to 300 °C, predicted conductance values decrease slightly. However, a significant rise in conductance was noted at 500 °C and further amplified at 700 °C. This sharp increase reflects increased electrical contact between the wire and the melt pool (Figure 11c). The influence of preheat temperature on electrical conductance, liquid bridge, and the boundary contour width of the melt pool's top surface

can be directly observed through in-process measurements. Conductance measurement and top-view imaging serve as sensing solutions that do not impose constraints on the mechanical flexibility of the processing head relative to the built geometry. Furthermore, these methods can be integrated into the head to shield them from the harsh interaction zone, which emits smoke and heat radiation.

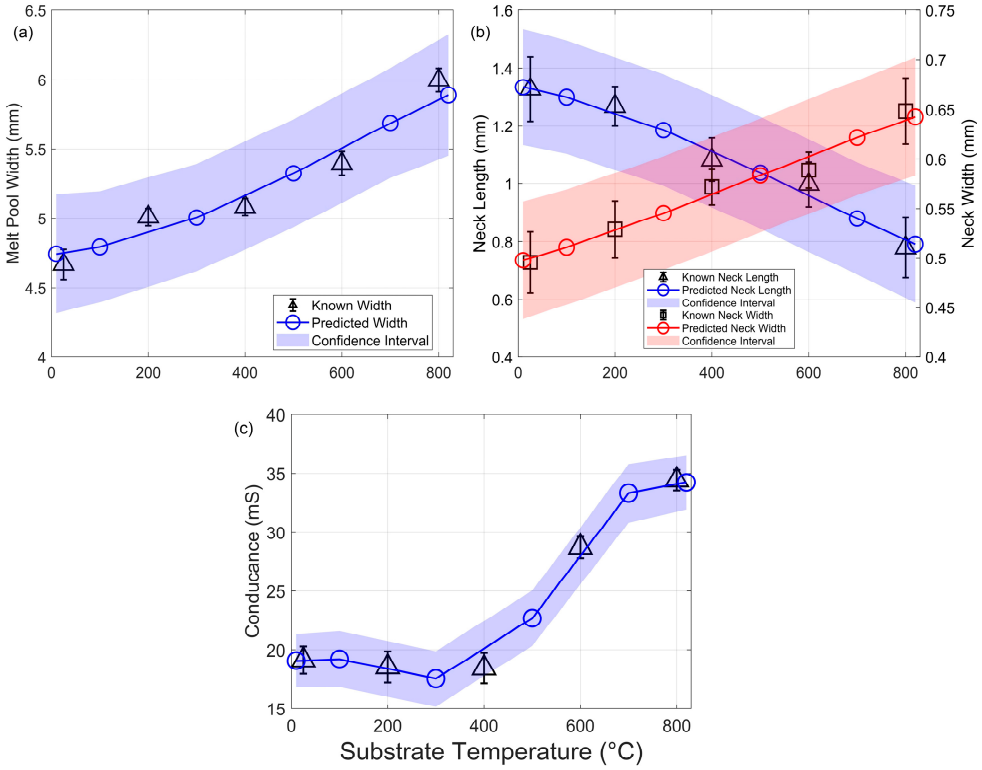


Figure 11. Effect of preheat temperature on (**a**) average melt pool width, (**b**) length and width of liquid bridge, (**c**) average electrical conductance, along with the Gaussian process regressor predictions. The blue circular symbols represent the predicted values, and the shaded blue region indicates the confidence interval.

The capability to collect data at varying sampling rates and through two fundamentally distinct sensing modes, scalar data from conductance measurements and field data from top-view imaging, facilitates sensor fusion. This robust in-process data can be leveraged for the automatic control of heat input. Conversely, side-view monitoring of the liquid bridge is less feasible in a general DED-LB/w processing scenario involving arbitrary geometries. This limitation arises from the constraints imposed by the imaging setup. While side-view monitoring provides valuable insights into the process and offers complementary data to the electrical conductance and melt pool width measurements, its utility for automation purposes during DED-LB/w processing is limited.

3.2. Bead Cross-Section Geometries

Figure 12 shows the relationship between substrate preheat temperature and cross-sectional measurements of deposited beads. The measurements include width, height, penetration depth, and total area (added metal plus penetration area). The width showed an increasing trend with the temperature rise, starting from approximately 4876 µm at 25 °C and peaking at 6192 µm at 800 °C (Figure 12a). The standard deviations were relatively small, except for the 800 °C point, which suggests that there was more variability at the highest temperature. This is likely due to the presence of oxide (Figure 7a) around the

deposited bead that causes uncertainty in cross-sectional width measurements compared to width measurements from top-view images.

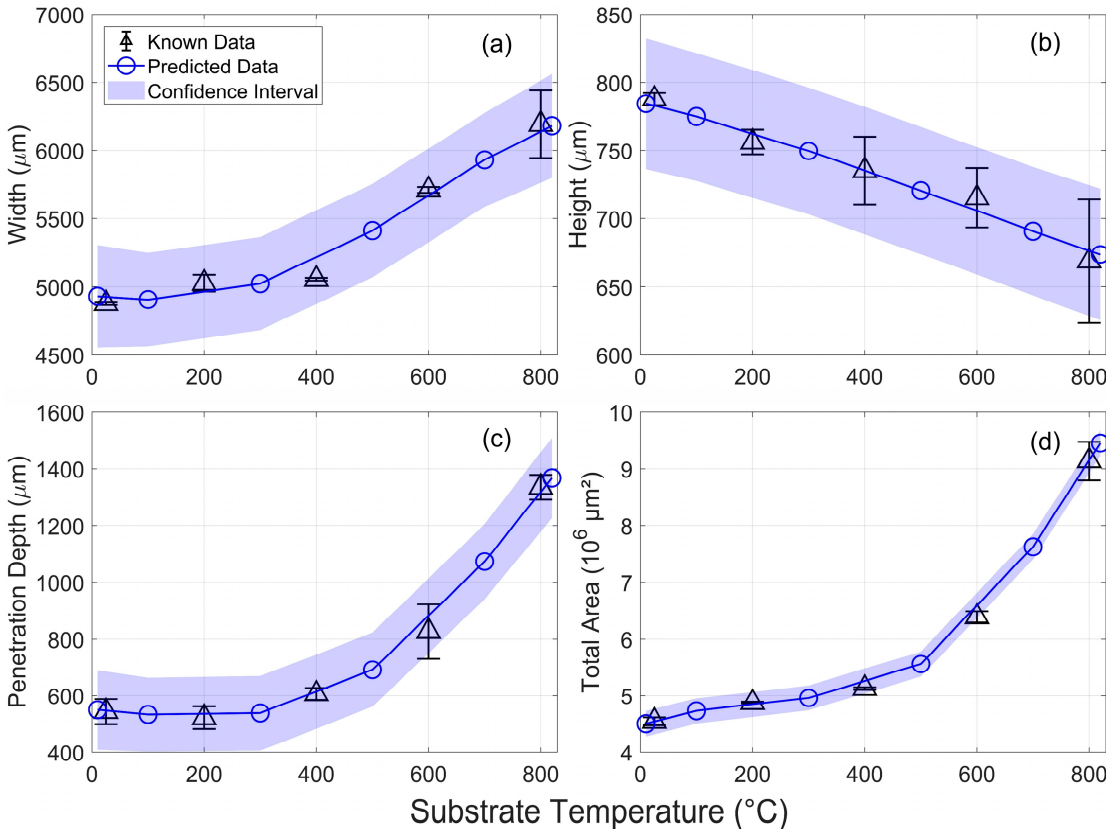


Figure 12. Bead cross-section features as a function of substrate preheat temperature, along with GPR predicted values for unseen temperatures (100 °C, 300 °C, 500 °C and 700 °C). The blue circular symbols represent the predicted values, the black triangular symbols represent the measured data with their standard deviations, and the shaded blue region indicates the confidence interval: (**a**) average and standard deviation of bead width, (**b**) average and standard deviation of bead height, (**c**) average and standard deviation of bead penetration depth, (**d**) average and standard of total cross-sectional area.

The bead height decreased consistently with preheat temperature, starting at 787 µm and reducing to 668 µm at 800 °C, see Figure 12b. This inverse relationship shows that higher temperatures lead to a flatter bead profile. The standard deviation was low, indicating consistent height measurements across beads. The penetration depth initially decreased slightly but began increasing significantly at higher temperatures, peaking at 1336 µm for 800 °C (Figure 12c). The increase at higher temperatures resulted in deeper fusion. The higher variability observed at 600 °C and 800 °C suggests inconsistency in penetration depth, caused by the variation in the position of the deepest penetration point across the bead cross-section, at these temperatures. The total cross-sectional area increased sharply with temperature, from approximately 4.5×10^6 µm^2 to 9.1×10^6 µm^2 (Figure 12d). The exponential-like growth in total area highlights the pronounced effect of preheat temperature on metal deposition. The trends suggest that higher temperatures promote metal spreading and deeper fusion. The measured total area became less consistent at elevated temperatures. This variability is likely attributed to the uneven penetration area, which influences the overall cross-sectional area of the bead.

The cross-section width predictions also showed a steady increase from 4906 µm at 100 °C to 5930 µm at 700 °C Figure 12a. This is consistent with the trend observed in the

melt pool top surface boundary contour width. Unlike the width, cross-section height is expected to decrease with temperature, from 774 µm at 100 °C to 690 µm at 700 °C. The most significant increase is observed in penetration depth, which rises dramatically from 532 µm at 100 °C to 1073 µm at 700 °C. Predictions also suggest that as the preheat temperature increased, the higher heat input resulted in a larger melt volume and larger cross-sectional area, which increased fusion in the deposited metal and the substrate. As penetration depth increases, the total area of added material and penetration area increase accordingly. The rate of change in all predicted cross-sectional features became steeper beyond 400 °C, reinforcing the idea that after a critical point, heat input increases. Bead characteristics measurements at higher preheat temperatures have a higher standard deviation, given that they are evaluated manually after solidification and depend on where the cross-section was obtained, making them subject to additional sources of uncertainty.

The in-process results indicate that the process dynamics change significantly at preheating temperatures above 400 °C. Beyond this critical threshold, Joule heating in the wire and melt pool becomes more pronounced (see Figure 13 showing how the electrical power increases from 400 °C), leading to a substantial rise in heat input. The mechanism behind this change is not trivially explained from the observations made, suggesting further analysis by means of fluid dynamic simulations. This is, however, out of the scope of this study. The practical implications of the observations are, however, that these conditions can be observed from the imaging and conductance measurements and thereby enable process monitoring and automatic control. The results also suggest that to maintain consistent heat and mass transfer, one should avoid a heat accumulation indicated by temperatures above the identified threshold. This can be performed by automatically lowering the heat input either by inter-pass waiting times or by adjusting the input energy through the laser power and travel speed modulation.

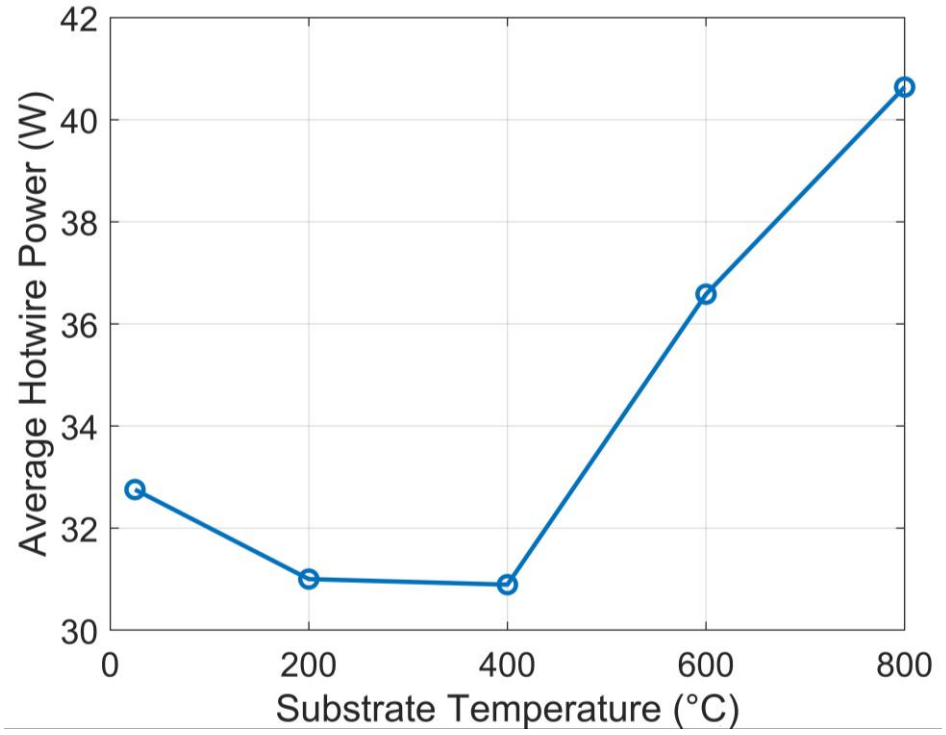


Figure 13. Average hotwire power as a function of substrate temperature.

While the general thermal trends such as larger melt pools and coarser microstructures with increasing preheat temperature are consistent with previous findings in powder- and arc-based DED systems, the present study reveals a coupling specific to the wire-fed

DED-LB/w process. The simultaneous increase in electrical conductance and stabilization of the liquid bridge at elevated substrate temperatures indicates that heat accumulation not only governs the thermal field but also influences mass-transfer stability via changes in electrical and geometric contact between the wire and melt pool. This coupling alters the distribution of Joule heating within the wire-melt region, reinforcing the temperature-dependent expansion of the molten pool and stabilizing metal transfer. Such interaction between heat accumulation and electrical-fluidic dynamics is absent in powder-fed systems, where the feedstock is discontinuous and electrically isolated. Consequently, this study elucidates how substrate preheating in DED-LB/w links heat accumulation to metal-transfer behavior, establishing a distinct interdependence not previously identified in other DED processes.

The post-process observations on the impact of preheat temperature on the melt pool volume and cross-sectional geometries are consistent with the in-process observations, thereby confirming the significant influence of preheat temperature on the deposition process.

It is feasible to establish empirical relationships between the in-process data and the cross-sectional geometries within the specific context of the conducted experiments. However, generalizing such empirical relationships to arbitrary deposition scenarios, different alloys, or varying power density distributions of the laser beam is unlikely to be achievable. To address this limitation, future work could focus on developing physics-informed machine learning models or multi-physics simulations that integrate both thermal and fluid dynamic effects. Such models would enable better generalization across different materials and process configurations by grounding data-driven predictions in fundamental heat transfer and melt pool dynamics. Alternatively, systematic experimental parameter mapping under controlled variations in alloy composition and beam profile could help identify transferable features and scaling laws to extend the applicability of empirical relationships.

3.3. Bead Microstructure and Hardness

Figure 14 shows OM micrographs of as-deposited bead microstructures on substrates with different preheat temperatures. All as-deposited beads mainly exhibit a columnar dendritic structure. The OM images clearly show that the size of these structures changes with the preheat temperature, becoming coarser as the preheat temperature increases. This qualitative observation is confirmed by quantitative measurements of the secondary dendrite arm spacing (SDAS), which progressively increases from approximately 2.5 to 7 μm at higher temperatures (Figure 15a). The predictions follow the same trend, showing a continued increase at even higher temperatures. This change in SDAS with the preheat temperatures can be explained based on the well-established relationship between the SDAS and cooling, as described in the following equation.

$$\lambda s = k_s \theta^{-n} \quad (1)$$

where λs is the SDAS, k_s and n are the material's constants, and θ is the cooling rate. According to Equation (1), a smaller cooling rate leads to a larger SDAS. The cooling rate is determined as the product of solidification velocity (R) and temperature gradient (G). i.e., G × R [28,29]. An extensive study by Köhnen et al. [30], through a simulation coupled with an experiment, showed that increasing the preheat temperature of the substrate before the deposition in the laser-based powder bed fusion (PBF-LB) process reduces both G and R, hence reducing the cooling rate of the melt pool during the solidification, which well-explains the increase in the size of the solidification substructure as the temperature of the substrate increases. The cooling rate in DED-LB/w is typically much slower than in

PBF-LB due to the larger heat input and melt volume. However, the same trends in both G and R can be observed.

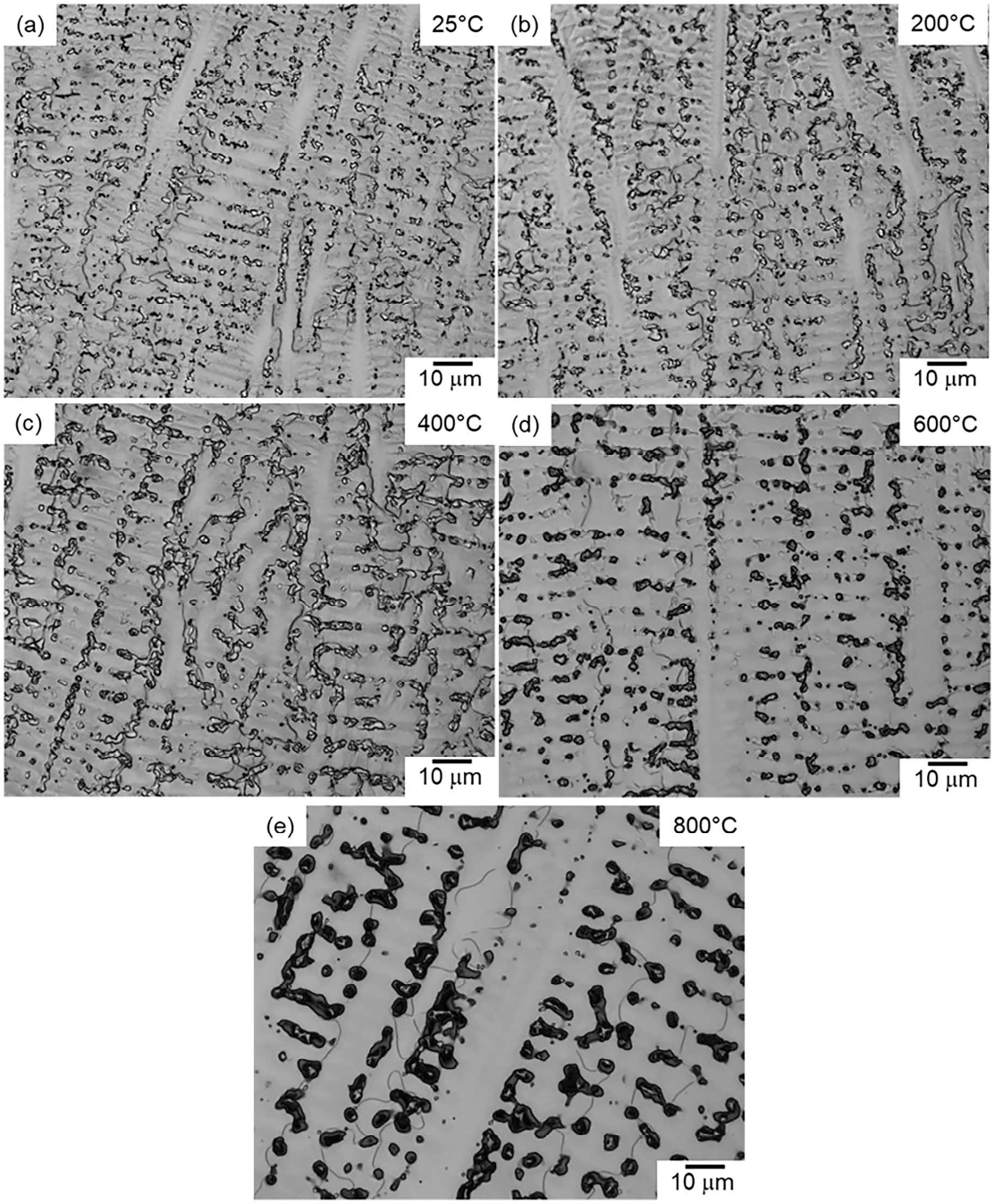


Figure 14. OM images of as-deposited bead microstructures on the substrates with different preheat temperatures: (**a**) 25 °C, (**b**) 200 °C, (**c**) 400 °C, (**d**) 600 °C, and (**e**) 800 °C.

In addition to the increase in the SDAS, an increase in the substrate's preheat temperature is also found to coarsen the grain size of the as-deposited bead microstructures. Figure 16 displays the EBSD inverse pole figure (IPF) colored maps of the microstructures, showing that all beads are primarily composed of columnar grains, and the width gradually increases with the substrate's preheat temperature. The change in the size of the columnar grain structure is reflected in the gradual increase in the length of the columnar grains, represented by the maximum Feret diameter obtained from the EBSD analysis, as shown in Figure 15b. The maximum Feret diameter corresponds to the largest chord length

across each grain and thus reasonably approximates the grain length in the additively manufactured microstructure. The Gaussian process model results are also depicted alongside the EBSD data, providing predicted values for unseen temperatures. The increase in the average grain size with increasing preheat temperature can also be linked to the decrease in the cooling rate. In solidification processing, it is generally observed that slower cooling rates increase the grain size of the as-solidified alloys, which is also the case for AM processes, as summarized by Murr [31] and Gorsse [32]. In AM, according to Zhang et al. [33], the mechanism of grain refinement caused by increased cooling rate is attributed to higher thermal undercooling, which promotes a higher degree of nucleation. Thus, decreasing the cooling rate by preheating the substrate will reduce the extent of undercooling, hence impeding the nucleation of grains, which ultimately coarsens the grain size. Grain size is well-known as one of the key factors affecting mechanical properties (toughness, fatigue, and yield strength), where the coarsening of the grains generally deteriorates these properties. Thus, from a process control standpoint, it becomes paramount to maintain the preheat temperature below the critical threshold by controlling the interlayer temperature to avoid inhomogeneous grain size throughout the building direction when performing multi-layer deposition.

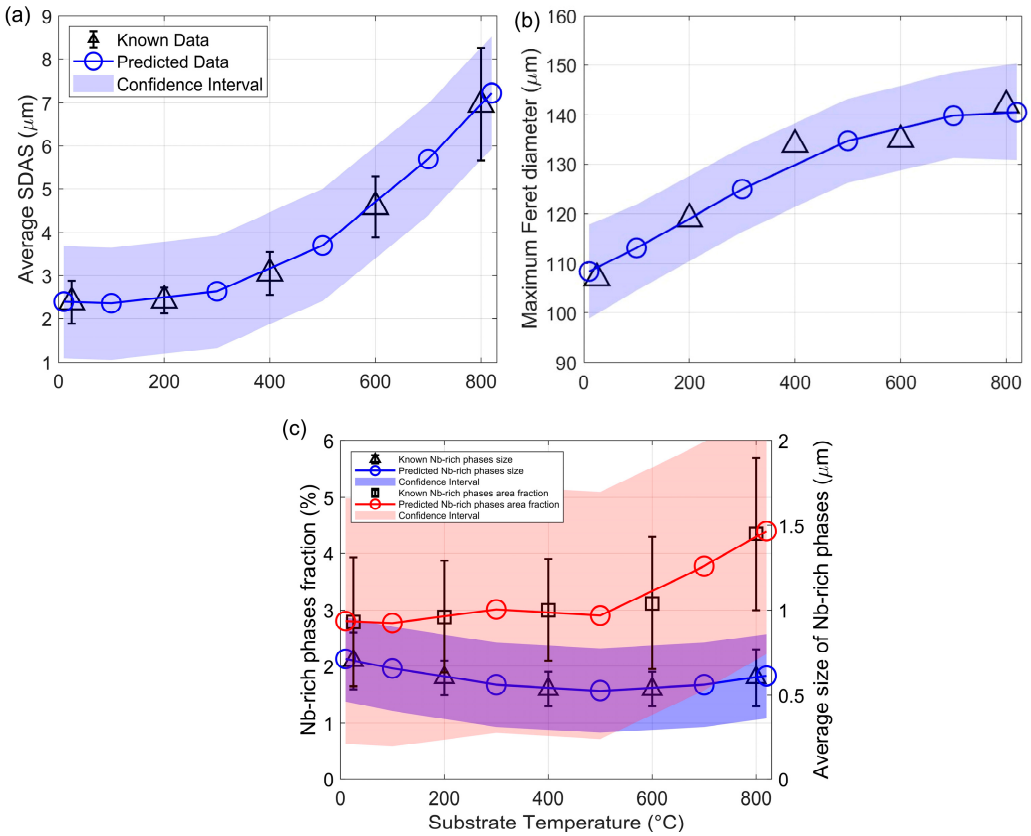


Figure 15. (**a**) Change in the SDAS of the as-deposited beads with different preheat temperatures, (**b**) Change in the maximum ferret diameter of grains of the as-deposited beads measured by EBSD analysis. The blue circular symbols represent the predicted values, the black triangular symbols represent the measured data, and the shaded blue region indicates the confidence interval, (**c**) The size and area fraction of Nb-rich phases (NbC and Laves) in the as-deposited bead microstructures on the substrates with different preheat temperatures.

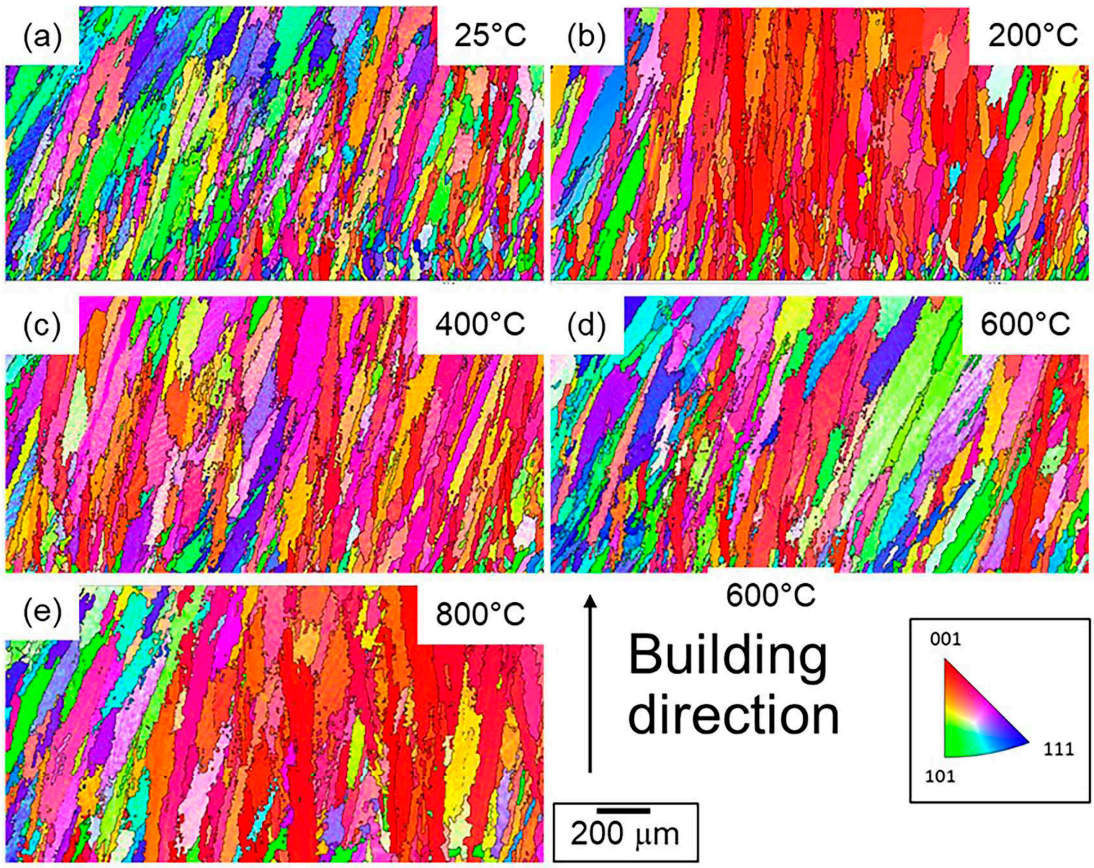


Figure 16. EBSD IPF maps that show the as-deposited microstructures on the substrates with different preheat temperatures: (**a**) 25 °C, (**b**) 200 °C, (**c**) 400 °C, (**d**) 600 °C, and (**e**) 800 °C.

Apart from forming the γ dendrite, the solidification of Alloy 718 also simultaneously involves a significant Nb microsegregation into the solidifying liquid, which eventually leads to the formation of Nb-rich eutectic secondary phases, i.e., NbC and Laves phase. The Laves phase particles are generally considered detrimental as they can adversely impact the mechanical properties, such as ductility, fracture toughness, tensile strength, and fatigue life, owing to their brittle nature [34]. The deleterious effect of the Laves phase is reported to be more pronounced in the coarse Laves particles than in the finer ones [35]. The size of the Laves phase also impacts the dissolution kinetics of the Laves phase during the post-heat treatment, where it takes longer to dissolve the coarser ones [36]. The size of Nb-rich phases in all samples was then measured using ImageJ software (ImageJ 1.54 g) based on the SEM backscatter electron (BSE) images. Ten images were used for the size and area fraction measurement for each deposited bead condition. The examples of the BSD micrographs of all as-deposited samples used for the measurement are shown in Figure 17. It can be seen from Figure 15c that the size of Nb-rich phases, which include both NbC and Laves phase, only slightly increases from 0.9 to 1 µm as the substrate's preheat temperature increases from 25 to 400 °C. Then, a sharp increase in the size of Nb-rich phases to 1.5 µm occurs when the substrate temperature reaches 800 °C. The reason for this abrupt change in Nb-rich phase size between 600 °C and 800 °C is not yet fully understood. Nonetheless, the general trend of increasing Nb-rich phase size with higher substrate temperatures can also be attributed to the lower cooling rate resulting from the preheating. It has been observed that the dendritic structure becomes coarser as the cooling rate decreases, based on the increase in the measured SDAS with increasing substrate temperature. Hence, as solidification progresses, the residual liquid gets confined within these coarser dendritic structures. Consequently, this leads to the formation of course NbC

and Laves phase particles. The increased size of the Laves phase in the bead deposited on the hotter substrate may also require careful consideration during the DED-LB/w of Alloy 718, especially if the interlayer temperature is not strictly controlled and exceeds 800 °C, since it may form an even coarser Laves phase and potentially deteriorate the mechanical properties.

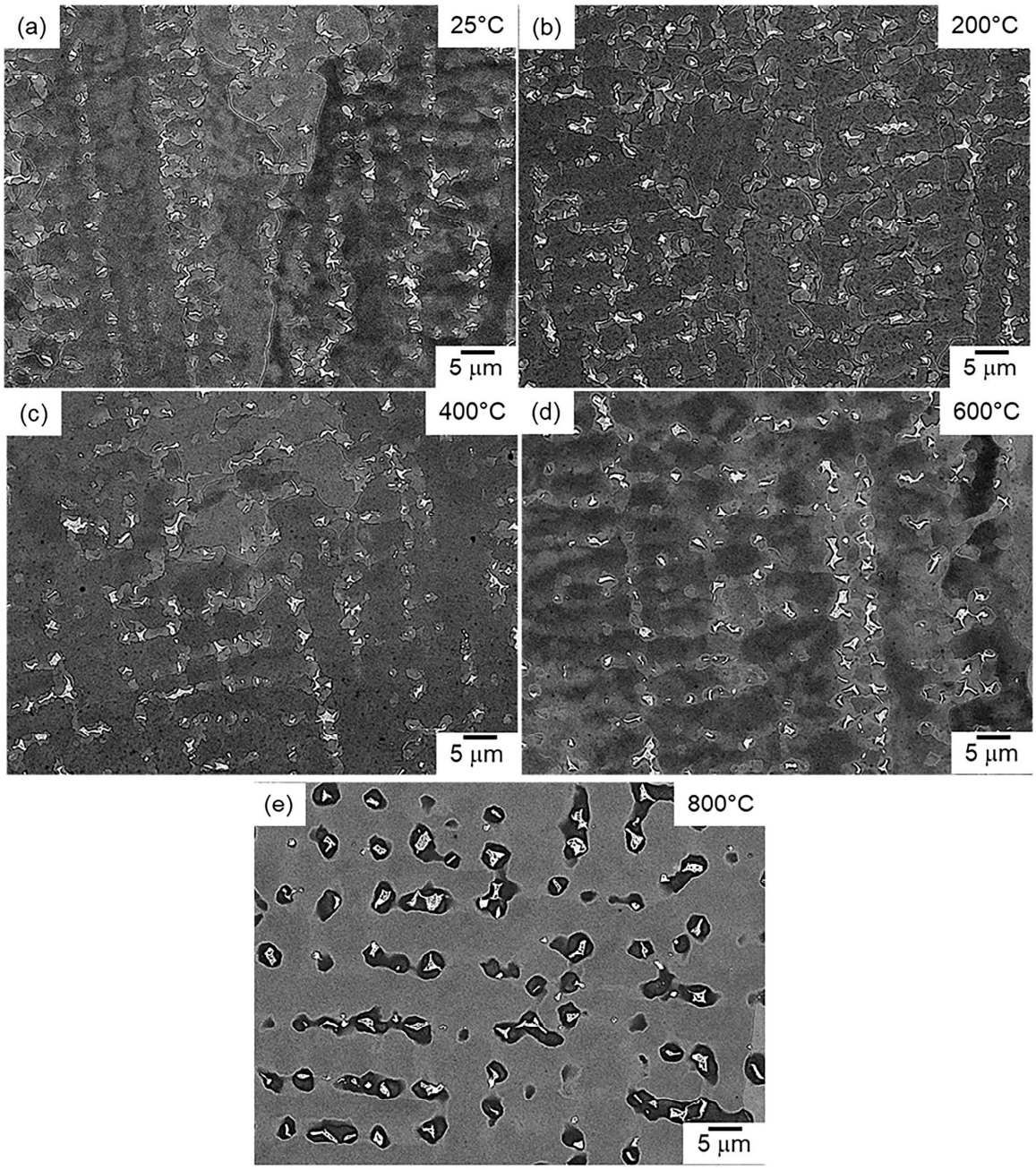


Figure 17. SEM BSE images that were used to measure the size and area fraction of Nb-rich secondary phases (NbC and Laves phase) in all as-deposited beads with different preheat temperatures: (**a**) 25 °C, (**b**) 200 °C, (**c**) 400 °C, (**d**) 600 °C, and (**e**) 800 °C.

The formation of these Nb-rich phases in the interdendritic region due to Nb microsegregation also typically results in the dendrite core composition being depleted in Nb, which is the essential element to form the γ'' phase during the post-age hardening treatment. The amount of the Nb-rich secondary phases is one of the parameters that can be used to scale the extent of Nb microsegregation during the solidification of Alloy 718 [36,37].

A larger area fraction of the phases could indicate a higher degree of microsegregation. In general, it is believed that a higher cooling rate during solidification would result in lower Nb microsegregation and, hence, a lower fraction of Nb-rich phases, as reported by Radhakrishna and Rao [37] through experiments and Kumara et al. [38] through phase field modeling. However, it was observed that the area fraction of the Nb-rich phases did not change notably as the substrate preheat temperature increased (Figure 15c). Note that although the area fraction of the phases in the beads that were deposited on the preheated substrate seems to be marginally lower compared to the one that was not preheated; nevertheless, considering the standard deviations that considerably overlap, the area fraction of the Nb-rich phases is arguably comparable across all samples.

To explain the similarity of the Nb-rich phase area fraction in all samples, the partition coefficient of Nb during solidification was assessed. The partition coefficient of a particular alloying element is an important solidification parameter that describes the extent of elemental microsegregation during solidification. The solidification follows the non-equilibrium mode at a rapid cooling rate, such as in AM processes. In this condition, the back diffusion is assumed to be negligible, and hence, the solute partitioning behavior into the interdendritic liquid is often approximated to follow the Scheil solidification equation.

$$C_s = kC_0[1 - f_s]^{(k-1)} \quad (2)$$

Here, *Cs* is the concentration of a particular element in the solidified solid or dendrite, C_0 is the alloy's chemical composition, f_s is the solid fraction, and k is the partition coefficient of the element. At the beginning of solidification (f_s = 0), supposing local equilibrium conditions and negligible undercooling at the dendrite tips, the first solid phase to form from the liquid, the dendrite core will contain a composition of kC_0. Consequently, the ratio between the dendrite core's composition and the alloy's nominal composition gives the initial k value at the onset of solidification. It is worth noting that the k value is not necessarily unchanging throughout the solidification. It, however, still provides valuable insight into the extent of microsegregation of alloying elements. The k value lower than unity shows that the element tends to partition or be rejected into the interdendritic liquid during solidification, whereas the value higher than unity suggests a preferential partitioning into the dendrite. The average concentrations of Nb in the dendrite core in all samples determined by SEM-EDS analysis on 15 points at the dendrite core's center and the corresponding kNb value are listed in Table 3. It is shown that kNb values are much less than unity and comparable across all samples with different substrates preheat temperatures, suggesting that the extent of microsegregation of Nb into the liquid in all samples is similar. The comparable k values of Nb could explain the similarities in the Nb-rich phase area fraction across all samples with different substrates' preheat temperatures.

Table 3. Average Nb concentration in the dendrite core (wt%) and Nb's corresponding calculated partition coefficients, i.e., k_{Nb}, in as-deposited bead microstructures on the substrates with different preheat temperatures.

Substrates Preheat Temperature (°C)	25	200	400	600	800
Average Nb concentration in the dendrite core (wt%)	2.17	2.21	2.18	2.16	2.13
Average k_{Nb}	0.43	0.43	0.43	0.42	0.42
Standard deviation of k_{Nb}	0.02	0.04	0.02	0.03	0.03

The nearly constant k values observed, regardless of substrate temperature (and thus the cooling rate), did not follow the general understanding of partitionless solidification in rapid solidification [39]. According to this concept, increasing the cooling rate may lead to

higher concentrations of Nb in the dendrite core (thus, a larger kNb value), bringing it closer to the alloy's bulk composition since the solutes are trapped at the moving solid/liquid interface due to their incomplete partitioning. Zhang et al. [40] found that the dendrite core in PBF-LB-built Alloy 718 contained the highest Nb concentration, followed by the DED-LB/p and cast counterparts, respectively. The PBF-LB typically results in the fastest cooling rates during solidification, while casting is the slowest. However, it should be noted that these three processes fundamentally differ, resulting in significantly different cooling rates. In this study, even though increasing the substrate temperature before deposition reduces the cooling rate, the process remains DED-LB/w with the same process parameters, which could not be as substantial as the difference in cooling rate due to entirely different processes, e.g., PBF-LB and DED-LB/p or DED-LB and cast. To estimate the cooling rate during solidification of Alloy 718 by PBF-LB, DED-LB/p, and cast, based on the study by Zhang et al. [40], Equation (1) was used. The SDAS of PBF-LB-built Alloy 718 reported by Zhang et al. [39] was at least one order and two orders of magnitude finer than the DED-LB/p built and cast counterparts, respectively. Using k_s and n of 62.9 and 0.407, respectively, for Alloy 718 [41], the corresponding cooling rates were estimated to differ by approximately two orders of magnitude between the PBF-LB-built and DED-LB/p-built materials, and similarly between the DED-LB/p-built and cast conditions. In contrast, the predicted cooling rates for beads deposited on substrates at 25 °C and 800 °C, based on the measured SDAS values, are approximately 3100 °C/s and 220 °C/s, respectively, representing only about one order of magnitude difference. This significantly smaller difference in cooling rate within the DED-LB/w process in comparison to the cooling rate difference among distinct manufacturing routes, i.e., PBF-LB-built and DED-LB/p, cast, supports the observation that the kNb and Nb-rich phase fraction remain nearly constant despite changes in substrate temperature. As a result, the reduction in cooling rate due to the higher preheat substrate temperatures could not be significant enough to increase the kNb value relative to decreasing the cooling rate by changing the process from PBF-LB to DED-LB/p or DED-LB/p to cast.

It is acknowledged that the highest substrate preheat temperature used in this study (800 °C) exceeds the range typically encountered during multi-layer DED-LB/w, where interlayer temperatures are generally below 600 °C. The inclusion of this extreme condition was deliberate: it was selected to establish the upper bound of thermal exposure and to examine the onset of microstructural degradation mechanisms such as coarsening of Laves phases and grain growth. By extending the preheating range to 800 °C, the experiment captured the transition from beneficial thermal moderation, reducing residual stresses and promoting melt pool stability, to detrimental overheating, where the solidification substructure and Nb-rich phase morphology degrade. In this sense, the 800 °C data does not represent a recommended processing condition but rather defines the process limit beyond which Alloy 718's microstructural integrity and mechanical performance begin to deteriorate. This boundary is essential for guiding practical process control, as it quantifies the temperature threshold that should not be exceeded to maintain the alloy's high-performance characteristics.

The hardness of all as-deposited beads with different substrate preheat temperatures revealed no significant difference in the average hardness across all samples, which are about 250 HV and 260 HV. The hardness of the as-deposited beads is very similar to that reported by Segerstark et al. [42] in their work on DED-LB/p-built Alloy 718. The similar hardness values can be explained by the comparable area fraction of Nb-rich phases, especially the Laves phase, across all the samples, since the Laves phase is a hard-brittle intermetallic constituent that can contribute to the average hardness of the sample. In addition, no evidence of hardening phases, i.e., γ' and γ'', is found in all samples in the

dendrite core or interdendritic region (Figure 18). Since the indentation diagonal in all samples was about 45 µm, which covers both dendritic core areas and interdendritic regions, the absence of both hardening phases in both regions further explains the similarity in hardness across all as-deposited beads. JMatPro simulation was carried out to calculate the CCT diagram of Alloy 718 based on the composition in the dendrite core and the interdendritic region. The compositions of these two regions were determined by SEM-EDS analysis. The CCT diagram (Figure 19) shows that even at a cooling rate of 1 °C/s, it does not touch the noses of γ' and γ'' precipitation. The cooling rate during the DED-LB/w process with different substrate preheating temperatures is estimated to be in the range of 200–3000 °C/s (between the cooling rate of DED-LB/p and casting), which explains the absence of the hardening phases in both regions.

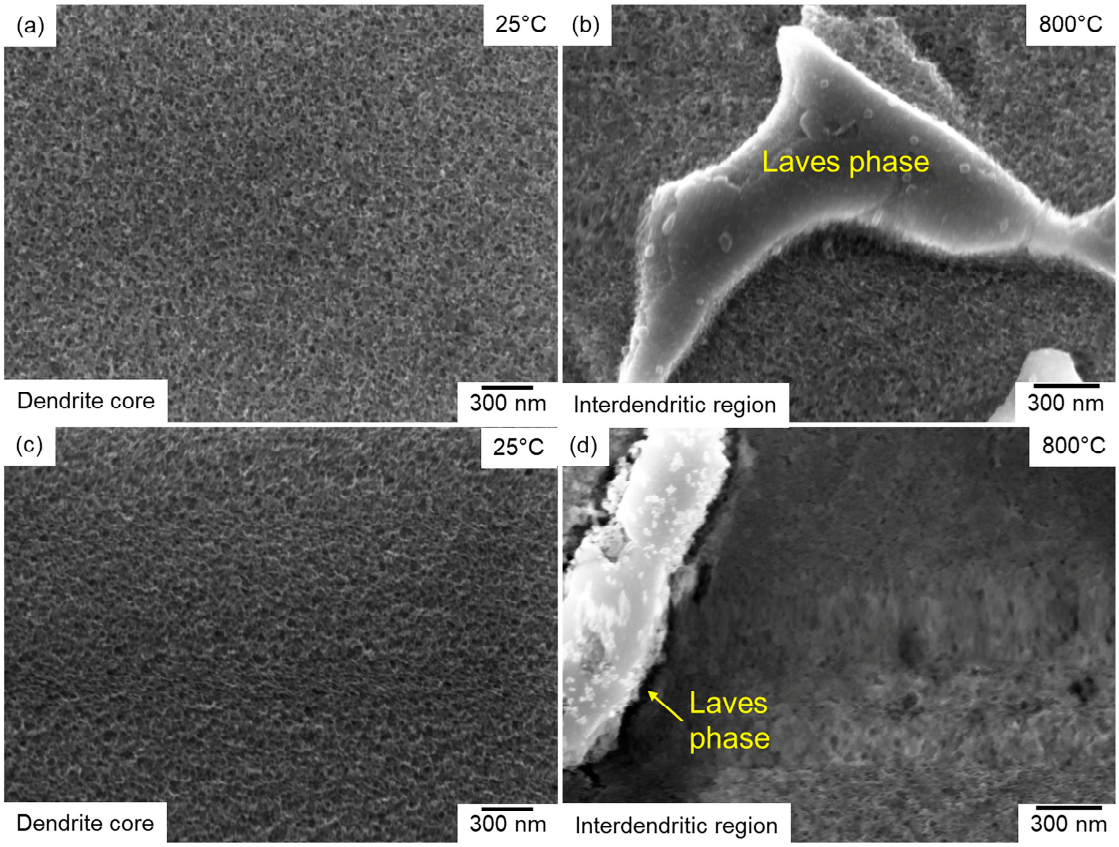


Figure 18. SEM In-lens images showing the absence of hardening phases in the dendrite core and interdendritic region of the deposited samples: (**a**,**c**) samples produced on substrate preheated to 25 °C, and (**b**,**d**) samples produced on substrate preheated to 800 °C.

The observations regarding the impact of preheat temperature on the resulting microstructure indicate that heat accumulation in DED-LB/w presents a challenge that must be mitigated through various heat input control strategies. These strategies are essential to ensure the structural integrity of as-built AM components and to minimize the need for time- and energy-intensive post-heat treatments.

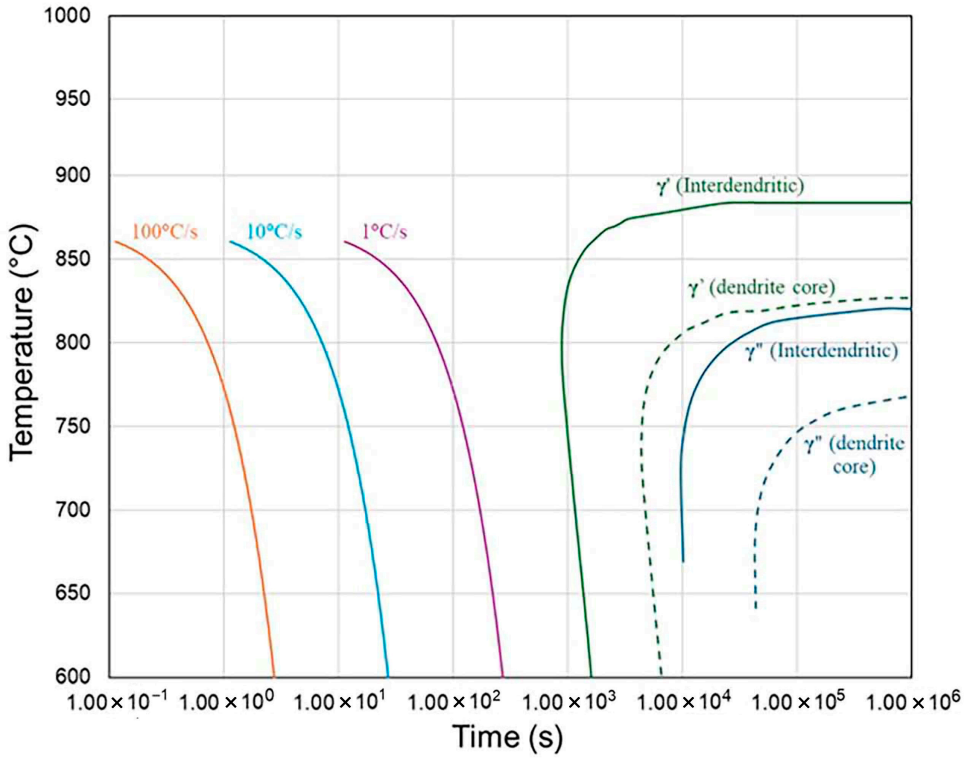


Figure 19. Calculated CCT diagram of Alloy 718 based on the composition of the dendrite core and interdendritic region.

4. Conclusions and Future Work

This study investigated the influence of substrate preheating to emulate heat accumulation during DED-LB/w, focusing on its effects on melt pool behavior, wire-melt pool interaction, bead geometry, and microstructure of Alloy 718 deposits. Experimental results demonstrated that increasing the substrate temperature led to larger melt pool volumes due to altered heat transfer dynamics and reduced cooling rates.

A critical threshold around 400 °C was identified, beyond which the effects of preheating became markedly stronger. Melt pool width increased gradually at lower preheats but expanded sharply at 600–800 °C. Electrical conductance measurements showed a similar threshold effect, remaining nearly constant below 400 °C but rising steeply thereafter, reflecting enlarged and steadier liquid bridges. Analysis of wire-melt pool interaction revealed that increasing preheat temperature shortened and thickened the liquid bridge, promoting a more stable metal transfer.

Microstructural analysis revealed coarser solidification features at higher preheats, including increased secondary dendrite arm spacing (SDAS) and larger columnar grains, consistent with reduced cooling rates. The size of Nb-rich secondary phases (NbC and Laves) increased significantly at 800 °C, though their area fraction and Nb partitioning coefficient (kNb) remained largely unchanged across all conditions. The enlarged Laves phases at higher preheats may pose challenges for mechanical performance and extend dissolution times during post-heat treatment. Despite these changes, hardness values remained stable at ~250–260 HV, owing to the absence of γ' and γ'' strengthening phases, which are suppressed at the high cooling rates (200–3000 °C/s) characteristic of DED-LB/w.

This work indicates a practical compromise for multi-layer DED-LB/w: maintain the interlayer temperature just below the identified threshold, i.e., ~300–380 °C. In this range, metal-transfer stability (shorter liquid bridge, steadier conductance) and geometric consistency are improved, while the rapid increase in melt-pool size, penetration, SDAS, grain size, and Laves coarsening observed at ≥400–600 °C are avoided.

Beyond confirming the established effects of preheating, this work provides new physical insight specific to the wire-fed DED-LB/w process. The concurrent trends observed in electrical conductance, melt pool geometry, and liquid bridge stability demonstrate a coupled mechanism, where increased preheat temperature enhances Joule heating and stabilizes metal transfer. This coupling, absent in powder-based systems, highlights the distinctive influence of wire-melt pool interaction on heat accumulation and process stability.

These findings highlight the necessity of precise thermal control during multi-layer DED-LB/w to ensure consistent geometry, microstructure, and mechanical properties. Future work should focus on strategies to mitigate heat accumulation, including interlayer time optimization and real-time monitoring of in-process signals (melt pool geometry, conductance). Such approaches will be critical to achieving reproducible performance in high-temperature Alloy 718 applications. The identification of the ~400 °C threshold enables the formulation of a practical process control strategy. Below this temperature, the melt pool geometry and conductance remain relatively constant; beyond it, both parameters exhibit rapid, non-linear growth. This makes the in-process electrical conductance signal a suitable feedback variable for closed-loop control. When the measured conductance begins to increase sharply, the controller could automatically reduce laser power or increase travel speed, thereby reducing the heat input and maintaining a smooth processing regime. Similarly, melt-pool width obtained from coaxial imaging could serve as a complementary feedback signal, with the goal of maintaining its width near the calibrated reference (≈4.7–5.0 mm). Together, these in-process observables define a quantitative basis for adaptive control aimed at preventing excessive heat accumulation and preserving the desired microstructure during multi-layer DED-LB/w deposition.

Author Contributions: Conceptualization, M.N. and F.S.; methodology, A.S., A.A. and F.S.; software, A.S.; validation, A.S. and A.A.; formal analysis, A.S.; investigation, A.S., A.A. and G.A.; resources, M.N. and F.S.; data curation, A.S.; writing—original draft preparation, A.S. and A.A.; writing—review and editing, A.S., M.N., F.S. and G.A.; visualization, A.S. and A.A.; supervision, M.N. and F.S.; project administration, M.N. and F.S.; funding acquisition, M.N. and F.S. All authors have read and agreed to the published version of the manuscript.

Funding: This research was funded by the project TANDEM (2021-03145) Vinnova under the SMART EUREKA cluster on advanced manufacturing program. It was also supported by grants from the Swedish Knowledge Foundation, project DEDICATE (20210094), which is gratefully acknowledged.

Data Availability Statement: The data that support the findings of this study are available from the corresponding author upon reasonable request. The dataset is not publicly available due to its large size and because part of the data was provided by an industrial partner.

Acknowledgments: The authors wish to express their sincere gratitude to Isabelle Choquet for her guidance in the interpretation of physical phenomena, and to Yongcui Mi for her input on image processing strategies. During the preparation of this manuscript, the authors used ChatGPT (OpenAI, GPT-3.5) to improve the clarity and readability of the text. The authors have carefully reviewed and edited the content generated and take full responsibility for the final version of the manuscript.

Conflicts of Interest: The authors declare no conflicts of interest. The funders had no role in the design of the study; in the collection, analyses, or interpretation of data; in the writing of the manuscript; or in the decision to publish the results.

Abbreviations

The following abbreviations are used in this manuscript:

AM	Additive Manufacturing
BSE	Backscatter Electron
CCT	Continuous Cooling Transformation
CI	Confidence Interval
DED	Directed Energy Deposition
DED-Arc	Directed Energy Deposition using wire arc
DED-LB	Directed Energy Deposition using Laser Beam
DED-LB/p	Directed Energy Deposition using Laser Beam and Powder
DED-LB/w	Directed Energy Deposition using Laser Beam and Wire
EBSD	Electron Backscatter Diffraction
EDS	Energy Dispersive Spectroscopy
GPR	Gaussian Process Regression
IPF	Inverse Pole Figure
Nb	Niobium
Ni-Fe	Nickel-Iron
OM	Optical Microscope
PBF-LB	Laser-based Powder Bed Fusion
PID	Proportional Integral Derivative
PLC	Programmable Logic Controller
SDAS	Secondary Dendrite Arm Spacing

References

1. Maffia, S.; Furlan, V.; Previtali, B. Coaxial and Synchronous Monitoring of Molten Pool Height, Area, and Temperature in Laser Metal Deposition. *Opt. Laser Technol.* **2023**, *163*, 109395. [CrossRef]
2. Ding, D.; Pan, Z.; Cuiuri, D.; Li, H. Wire-Feed Additive Manufacturing of Metal Components: Technologies, Developments and Future Interests. *Int. J. Adv. Manuf. Technol.* **2015**, *81*, 465–481. [CrossRef]
3. Hagqvist, P. Non-Intrusive Instrumentation and Estimation: Applications for Control of an Additive Manufacturing Process. Ph.D. Thesis, Chalmers University of Technology, Gothenburg, Sweden, 2015.
4. Kisielewicz, A.; Pandian, K.T.; Sthen, D.; Hagqvist, P.; Bermejo, M.A.V.; Sikström, F.; Ancona, A. Hot-Wire Laser-Directed Energy Deposition: Process Characteristics and Benefits of Resistive Pre-Heating of the Feedstock Wire. *Metals* **2021**, *11*, 634. [CrossRef]
5. Lee, S.H. CMT-Based Wire Arc Additive Manufacturing Using 316L Stainless Steel: Effect of Heat Accumulation on the Multi-Layer Deposits. *Metals* **2020**, *10*, 278. [CrossRef]
6. Halder, R.; Pistorius, P.C.; Blazanin, S.; Sardey, R.P.; Quintana, M.J.; Pierson, E.A.; Verma, A.K.; Collins, P.C.; Rollett, A.D. The Effect of Interlayer Delay on the Heat Accumulation, Microstructures, and Properties in Laser Hot Wire Directed Energy Deposition of Ti-6Al-4V Single-Wall. *Materials* **2024**, *17*, 3307. [CrossRef]
7. Hatala, G.W.; Reutzel, E.; Wang, Q. An Investigation of Thermomechanical Behavior in Laser Hot Wire Directed Energy Deposition of NAB: Finite Element Analysis and Experimental Validation. *Metals* **2024**, *14*, 1143. [CrossRef]
8. Singh, S.; Jinoop, A.N.; Tarun Kumar, G.T.A.; Palani, I.A.; Paul, C.P.; Prashanth, K.G. Effect of Interlayer Delay on the Microstructure and Mechanical Properties of Wire Arc Additive Manufactured Wall Structures. *Materials* **2021**, *14*, 4187. [CrossRef]
9. Ekanayaka, V.; Lachmayer, L.; Raatz, A.; Hürkamp, A. Approach to Optimize the Interlayer Waiting Time in Additive Manufacturing with Concrete Utilizing FEM Modeling. *Procedia CIRP* **2022**, *109*, 562–567. [CrossRef]
10. Ding, D.; Wu, B.; Pan, Z.; Qiu, Z.; Li, H. Wire Arc Additive Manufacturing of Ti6AL4V Using Active Interpass Cooling. *Mater. Manuf. Process.* **2020**, *35*, 845–851. [CrossRef]
11. Hagenlocher, C.; O'Toole, P.; Xu, W.; Brandt, M.; Easton, M.; Molotnikov, A. Heat Accumulation in Laser Additive Manufacturing Processes and Its Effect on Local Solidification. *Procedia CIRP* **2022**, *111*, 176–179. [CrossRef]
12. Rosli, N.A.; Alkahari, M.R.; bin Abdollah, M.F.; Maidin, S.; Ramli, F.R.; Herawan, S.G. Review on Effect of Heat Input for Wire Arc Additive Manufacturing Process. *J. Mater. Res. Technol.* **2021**, *11*, 2127–2145. [CrossRef]
13. Wu, B.; Pan, Z.; Ding, D.; Cuiuri, D.; Li, H. Effects of Heat Accumulation on Microstructure and Mechanical Properties of Ti6Al4V Alloy Deposited by Wire Arc Additive Manufacturing. *Addit. Manuf.* **2018**, *23*, 151–160. [CrossRef]
14. Wu, B.; Ding, D.; Pan, Z.; Cuiuri, D.; Li, H.; Han, J.; Fei, Z. Effects of Heat Accumulation on the Arc Characteristics and Metal Transfer Behavior in Wire Arc Additive Manufacturing of Ti6Al4V. *J. Mater. Process Technol.* **2017**, *250*, 304–312. [CrossRef]

15. Gao, Z.; Shi, H.; Yang, X.; Lyu, F.; Wang, L.; Zhan, X. Influence of Heat Accumulation on the Distribution Uniformity of Microstructure and Mechanical Properties of Laser Additive Manufacturing Joint of 80 Mm Thick Ti6Al4V Titanium Alloy Plates. *J. Mater. Process Technol.* **2022**, *310*, 117774. [CrossRef]
16. Hwang, S.; Oh, W.J.; Kim, D.H.; Kim, J.G.; Oh, J.S.; Nam, T.H.; Kim, C.S.; Lee, T. Optimizing Interlayer Cooling for SUS316L Thin Wall Fabricated by Directed Energy Deposition. *J. Mater. Res. Technol.* **2023**, *23*, 5239–5245. [CrossRef]
17. Hagenlocher, C.; O'Toole, P.; Xu, W.; Brandt, M.; Easton, M.; Molotnikov, A. Analytical Modelling of Heat Accumulation in Laser Based Additive Manufacturing Processes of Metals. *Addit. Manuf.* **2022**, *60*, 103263. [CrossRef]
18. Jin, Z.; Kong, X.; Ma, L. Investigating the Impact of Substrate Preheating on the Thermal Flow and Microstructure of Laser Cladding of Nickel-Based Superalloy. *Materials* **2024**, *17*, 399. [CrossRef]
19. Davis, J.R. *Nickel, Cobalt, and Their Alloys*; ASM International: Almere, The Netherlands, 2000.
20. Andersson, J. Fabrication and Weldability Aspects of Ni- and Ni–Fe Based Superalloys—A Review. In Proceedings of the 10th International Symposium on Superalloy 718 and Derivatives, San Diego, CA, USA, 19–23 March 2023; Springer Nature: Cham, Switzerland, 2023.
21. Permanova. Available online: https://www.permanova.se/ (accessed on 15 September 2025).
22. Hagqvist, P.; Heralić, A.; Christiansson, A.K.; Lennartson, B. Resistance Based Iterative Learning Control of Additive Manufacturing with Wire. *Mechatronics* **2015**, *31*, 116–123. [CrossRef]
23. Schulz, E.; Speekenbrink, M.; Krause, A. A Tutorial on Gaussian Process Regression: Modelling, Exploring, and Exploiting Functions. *J. Math. Psychol.* **2018**, *85*, 1–16. [CrossRef]
24. Mehrotra, R.; Namuduri, K.R.; Ranganathan, N. Gabor Filter-Based Edge Detection. *Pattern Recognit.* **1992**, *25*, 1479–1494. [CrossRef]
25. Jain, A.K.; Farrokhnia, F. Unsupervised Texture Segmentation Using Gabor Filters. *Pattern Recognit.* **1991**, *24*, 1167–1186. [CrossRef]
26. Mi, Y.; Sikström, F.; Angelastri, L.; Guglielmi, P.; Palumbo, G.; Ancona, A. Improving Laser Directed Energy Deposition with Wire Feed-Stock through Beam Shaping with a Deformable Mirror. *Opt. Lasers Eng.* **2025**, *185*, 108716. [CrossRef]
27. Chen, Q.; Zhao, Y.; Strayer, S.; Zhao, Y.; Aoyagi, K.; Koizumi, Y.; Chiba, A.; Xiong, W.; To, A.C. Elucidating the Effect of Preheating Temperature on Melt Pool Morphology Variation in Inconel 718 Laser Powder Bed Fusion via Simulation and Experiment. *Addit. Manuf.* **2021**, *37*, 101642. [CrossRef]
28. Pottlacher, G.; Hosaeus, H.; Kaschnitz, E.; Seifter, A. Thermophysical Properties of Solid and Liquid Inconel 718 Alloy. *Scand. J. Metall.* **2002**, *31*, 161–168. [CrossRef]
29. Bontha, S.; Klingbeil, N.W.; Kobryn, P.A.; Fraser, H.L. Thermal Process Maps for Predicting Solidification Microstructure in Laser Fabrication of Thin-Wall Structures. *J. Mater. Process Technol.* **2006**, *178*, 135–142. [CrossRef]
30. Köhnen, P.; Létang, M.; Voshage, M.; Schleifenbaum, J.H.; Haase, C. Understanding the Process-Microstructure Correlations for Tailoring the Mechanical Properties of L-PBF Produced Austenitic Advanced High Strength Steel. *Addit. Manuf.* **2019**, *30*, 100914. [CrossRef]
31. Murr, L.E. A Metallographic Review of 3D Printing/Additive Manufacturing of Metal and Alloy Products and Components. *Metallogr. Microstruct. Anal.* **2018**, *7*, 103–132. [CrossRef]
32. Gorsse, S.; Hutchinson, C.; Gouné, M.; Banerjee, R. Additive Manufacturing of Metals: A Brief Review of the Characteristic Microstructures and Properties of Steels, Ti-6Al-4V and High-Entropy Alloys. *Sci. Technol. Adv. Mater.* **2017**, *18*, 584–610. [CrossRef]
33. Zhang, D.; Prasad, A.; Bermingham, M.J.; Todaro, C.J.; Benoit, M.J.; Patel, M.N.; Qiu, D.; StJohn, D.H.; Qian, M.; Easton, M.A. Grain Refinement of Alloys in Fusion-Based Additive Manufacturing Processes. *Metall. Mater. Trans. A Phys. Metall. Mater. Sci.* **2020**, *51*, 4341–4359. [CrossRef]
34. Schirra, J.J.; Caless, R.H.; Hatala, R.W. The Effect of Laves Phase on the Mechanical Properties of Wrought and Cast + HIP Inconel 718. *Superalloys* **1991**, 375–388. [CrossRef]
35. Sui, S.; Tan, H.; Chen, J.; Zhong, C.; Li, Z.; Fan, W.; Gasser, A.; Huang, W. The Influence of Laves Phases on the Room Temperature Tensile Properties of Inconel 718 Fabricated by Powder Feeding Laser Additive Manufacturing. *Acta Mater.* **2019**, *164*, 413–427. [CrossRef]
36. Kumara, C.; Deng, D.; Hanning, F.; Raanes, M.; Moverare, J.; Nylén, P. Predicting the Microstructural Evolution of Electron Beam Melting of Alloy 718 with Phase-Field Modeling. *Metall. Mater. Trans. A Phys. Metall. Mater. Sci.* **2019**, *50*, 2527–2537. [CrossRef]
37. Radhakrishna, C.; Prasad Rao, K. The Formation and Control of Laves Phase in Superalloy 718 Welds. *J. Mater. Sci.* **1997**, *32*, 1977–1984. [CrossRef]
38. Kumara, C.; Segerstark, A.; Hanning, F.; Dixit, N.; Joshi, S.; Moverare, J.; Nylén, P. Microstructure Modelling of Laser Metal Powder Directed Energy Deposition of Alloy 718. *Addit. Manuf.* **2019**, *25*, 357–364. [CrossRef]
39. Trivedi, R.; Kurz, W. Solidification Microstructures: A Conceptual Approach. *Acta Metall. Mater.* **1994**, *42*, 15–23. [CrossRef]

40. Zhang, S.; Wang, L.; Lin, X.; Yang, H.; Huang, W. The Formation and Dissolution Mechanisms of Laves Phase in Inconel 718 Fabricated by Selective Laser Melting Compared to Directed Energy Deposition and Cast. *Compos. B Eng.* **2022**, *239*, 109994. [CrossRef]
41. Ling, L.; Han, Y.; Zhou, W.; Gao, H.; Shu, D.; Wang, J.; Kang, M.; Sun, B. Study of Microsegregation and Laves Phase in INCONEL718 Superalloy Regarding Cooling Rate During Solidification. *Metall. Mater. Trans. A Phys. Metall. Mater. Sci.* **2015**, *46*, 354–361. [CrossRef]
42. Segerstark, A.; Andersson, J.; Svensson, L.E.; Ojo, O. Microstructural Characterization of Laser Metal Powder Deposited Alloy 718. *Mater. Charact.* **2018**, *142*, 550–559. [CrossRef]

Disclaimer/Publisher's Note: The statements, opinions and data contained in all publications are solely those of the individual author(s) and contributor(s) and not of MDPI and/or the editor(s). MDPI and/or the editor(s) disclaim responsibility for any injury to people or property resulting from any ideas, methods, instructions or products referred to in the content.